Geophysical Journal International

Geophys. J. Int. (2025) **242,** 1–26
Advance Access publication 2025 May 21
Research paper

https://doi.org/10.1093/gji/ggaf184

Three-dimensional wave propagation and earthquake dynamic rupture simulations in complex poroelastic media

Sebastian Wolf,[1] Alice-Agnes Gabriel ,[2,3] Martin Galis ,[4,5] Peter Moczo ,[4,5] David Gregor[6] and Michael Bader[1]

[1] *Department of Computer Science, Technical University of Munich,* 80290 *Munich, Germany*
[2] *Scripps Institution of Oceanography, University of California San Diego,* 9500 *Gilman Drive La Jolla, CA* 92093-0225*, USA. E-mail: algabriel@ucsd.edu*
[3] *Department of Earth and Environmental Sciences, Ludwig—Maximilians—Universität München, Theresienstraße* 41 80333 *Munich, Germany*
[4] *Faculty of Mathematics, Physics and Informatics, Comenius University in Bratislava, Mlynska dolina F*1 842 48 *Bratislava, Slovakia*
[5] *Geophysical Institute, Slovak Academy of Sciences, Dúbravská cesta* 9, 840 05 *Bratislava, Slovakia*
[6] *Université Grenoble Alpes, University of Savoie Mont Blanc, CNRS, IRD, University of Gustave Eiffel, ISTerre, Grenoble, France*

Accepted 2025 May 12. Received 2025 April 17; in original form 2024 September 26

SUMMARY

Numerical simulations of earthquakes and seismic wave propagation require accurate material models of the solid Earth. In contrast to purely elastic rheology, poroelasticity accounts for pore fluid pressure and fluid flow in porous media. Poroelastic effects can alter both the seismic wave field and the dynamic rupture characteristics of earthquakes. For example, the presence of fluids may affect cascading multifault ruptures, potentially leading to larger-than-expected earthquakes. However, incorporating poroelastic coupling into the elastodynamic wave equations increases the computational complexity of numerical simulations compared to elastic or viscoelastic material models, as the underlying partial differential equations become stiff. In this study, we use a Discontinuous Galerkin solver with Arbitrary High-Order DERivative time stepping of the poroelastic wave equations implemented in the open-source software SeisSol to simulate 3-D complex seismic wave propagation and 3-D dynamic rupture in poroelastic media. We verify our approach for double-couple point sources using independent methods including a semi-analytical solution and a finite-difference scheme and a homogeneous full-space and a poroelastic layer-over-half-space model, respectively. In a realistic carbon capture and storage reservoir scenario at the Sleipner site in the Utsira Formation, Norway, we model 3-D wave propagation through poroelastic sandstone layers separated by impermeable shale. Our results show a sudden change in the pressure field across material interfaces, which manifests as a discontinuity when viewed at the length scale of the dominant wavelengths of *S* or fast *P* waves. Accurately resolving the resulting steep pressure gradient dramatically increases the computational demands, requiring high-resolution modelling. We show that the Gassmann elastic equivalent model yields almost identical results to the fully poroelastic model when focusing solely on solid particle velocities. We extend this approach using suitable numerical fluxes to 3-D dynamic rupture simulations in complex fault systems, presenting the first 3-D scenarios that combine poroelastic media with geometrically complex, multifault rupture dynamics and tetrahedral meshes. Our findings reveal that, in contrast to modelling wave propagation only, poroelastic materials significantly alter rupture characteristics compared to using elastic equivalent media since the elastic equivalent fails to capture the evolution of pore pressure. Particularly in fault branching scenarios, the Biot coefficient plays a key role in either promoting or inhibiting fault activation. In some cases, ruptures are diverted to secondary faults, while in others, poroelastic effects induce rupture arrest. In a fault zone dynamic rupture model, we find poroelasticity aiding pulse-like rupture. A healing front is induced by the reduced pore pressure due to reflected waves from the boundaries of the poroelastic damage zone. Our results highlight that poroelastic effects are important for realistic simulations of seismic waves and earthquake rupture dynamics. In particular, our poroelastic simulations may offer new insights on the complexity of multifault rupture dynamics, fault-to-fault interaction and seismic wave propagation in realistic models of the Earth's subsurface.

Key words: Permeability and porosity; Computational seismology; Earthquake dynamics; Rheology and friction of fault zones; Wave propagation; Wave scattering and diffraction.

1 INTRODUCTION

Poroelasticity integrates concepts from elasticity, fluid dynamics and geomechanics and enables the coupling of fluid pressure and deformation in porous media, which is important for applications ranging from seismic exploration to monitoring of geological reservoirs and earthquake physics (e.g. Carcione *et al.* 2010). Poroelastic effects are modulated by the porosity, permeability and fluid saturation of rocks and can affect the seismic wave field. In addition, the interaction between fluid flow and earthquake fault slip can affect dynamic rupture characteristics in earthquake simulations. Despite remarkable efforts in the laboratory and field (e.g. Berryman 1980; Plona 1980; Carcione 2015), observing poroelastic effects remains a challenge, motivating numerical simulations to accurately represent the interaction between fluid flow and solid deformation in heterogeneous geological settings.

However, to capture these interactions at realistic scales and resolution, numerical simulations require large computational resources. For example, during a reflection and/or transition of seismic waves at/through material interfaces and/or at the free surface in poroelastic materials, a slow diffusive *P* wave is generated, which has a small wavelength compared to the fast *P* wave and *S* wave, and attenuates quickly with distance from its origin (Dutta & Odé 1983). To accurately model the slow *P* wave at an interface or free surface, a fine resolution is required to resolve the relative fluid velocities (Wolf *et al.* 2022).

Poroelastic media can be described by Biot's equations (Biot 1956a, b, c, 1962), and poroelastic effects have been considered in numerical simulations of seismic wave propagation for more than three decades (e.g. Zhu & McMechan 1991; Masson *et al.* 2006; De Barros *et al.* 2010; Morency *et al.* 2011; Moczo *et al.* 2019; Gregor *et al.* 2021, 2022). Earthquake dynamic rupture simulations (Harris *et al.* 2011, 2018; Ramos *et al.* 2022) account for the nonlinear coupling of seismic wave propagation and frictional failure along faults and are a mature tool to advance the understanding of earthquake physics and physics-based seismic hazard assessment (e.g. Oglesby *et al.* 1998; Harris *et al.* 2021; Gabriel *et al.* 2023). While a variety of numerical implementations exist (e.g. Virieux & Madariaga 1982; Cruz-Atienza & Virieux 2004; Kaneko *et al.* 2008; Barall 2009; Pelties *et al.* 2012b; Duru & Dunham 2016; Okubo *et al.* 2020; Gabriel 2021; Hayek *et al.* 2023), dynamic simulations of earthquake rupture typically assume simplified (elastic, viscoelastic, or visco-elasto-plastic) off-fault material rheologies (e.g. Uphoff *et al.* 2017; Taufiqurrahman *et al.* 2022).

New opportunities to address these challenges have emerged with recent advances in high performance computing and the development of advanced numerical methods. It is now possible to simulate earthquake rupture scenarios in poroelastic materials: for example, Pampillón *et al.* (2018, 2023) and Li & Zhang (2023) demonstrate how pore pressure effects can additionally weaken a fault, facilitating the transition to supershear rupture analysing planar faults in homogeneous media. Pampillón *et al.* (2018, 2023) use COMSOL, a commercial finite element solver, while Li & Zhang (2023) develop a solver based on a boundary integral equations method. Recently, Wolf *et al.* (2022) developed an efficient high-order accurate ADER-DG (Arbitrary high-order DERivative Discontinuous Galerkin) scheme for the simulation of seismic waves in 3-D poroelastic media, extending the approach introduced by de la Puente (2008). The work presented here extends the capabilities of the ADER-DG method by incorporating double-couple moment tensor point sources and dynamic rupture embedded in a poroelastic medium. We apply our approach to simulate seismic wave propagation in a complex 3-D geological model and dynamic rupture simulations accounting for fault branching and fault zone effects.

The remainder of this paper is organized as follows: In Section 2.1, we review the theoretical frameworks underlying the poroelastic elastodynamic wave equations and dynamic rupture models. In Section 2.2, we briefly summarize the discontinuous Galerkin approach to discretize the poroelastic wave equation. We study poroelastic effects for a moment tensor point source in Section 3.1, focusing on the behaviour of pore pressure at material interfaces. We verify the correct implementation of double couple point sources in a homogeneous full-space and in a layer-over-half-space model in comparison to semi-analytical and finite-difference results, respectively. Then, we model the seismic wave field in a realistic carbon capture and storage (CCS) reservoir. In Section 3.2, we investigate the effects of poroelasticity on 3-D earthquake dynamics for a branching fault model and a fault embedded in a fault damage zone. We discuss our findings, implications and future research directions that our work motivates in Section 4.

2 METHODS

2.1 Statement of the problem

In the following, we briefly summarize the equations governing elastodynamic wave propagation in poroelastic media. Furthermore, we summarize the dynamic rupture source mechanism, which couples seismic wave propagation and frictional failure along pre-defined faults.

A poroelastic medium consists of an elastic matrix, which represents a solid material. The pore space within this matrix is saturated with a fluid. We follow Biot's model that describes the interaction of the matrix and fluid by considering a homogenized material (Biot 1956a, b, c, 1962). As principal quantities, we define the total stress of the combined material σ_{ij}, the solid particle velocities of the matrix u, v, w, the fluid pressure p and the relative fluid velocities $u_\mathrm{f}, v_\mathrm{f}, w_\mathrm{f}$. We then solve the poroelastic wave equation in the first-order form as given by de la Puente *et al.* (2008):

$$\frac{\partial Q_p}{\partial t} + A_{pq}\frac{\partial Q_q}{\partial x} + B_{pq}\frac{\partial Q_q}{\partial y} + C_{pq}\frac{\partial Q_q}{\partial z} = E_{pq}Q_q\,. \tag{1}$$

The vector $\vec{Q} = \left(\sigma_{xx}, \sigma_{yy}, \sigma_{zz}, \sigma_{xy}, \sigma_{yz}, \sigma_{xz}, u, v, w, p, u_\mathrm{f}, v_\mathrm{f}, w_\mathrm{f}\right)$ comprises all unknowns, we use Q_p to refer to the p^{th} element of the vector. The elements of the flux matrices $A, B, C \in \mathbb{R}^{13\times13}$ and the source matrix $E \in \mathbb{R}^{13\times13}$ are detailed in Appendix A. Eq. (1) is written in Einstein notation, that is, a repeated index implies summation over this index. For more details on the use of this notation within SeisSol, see Uphoff & Bader (2020).

The poroelastic material is described by a total of ten different material parameters. The solid matrix is characterized by its density ρ_S and the bulk modulus of the solid material K_S. The drained matrix behaves like an elastic body, that is, its response to deformation is described by the two Lamé parameters λ_M and μ_M. The matrix and the geometry of the pore space are characterized by the porosity

ϕ, the permeability κ and the tortuosity T. The fluid, which fills the pores, is defined by its bulk modulus K_F, the density ρ_F and its viscosity ν. A detailed overview of the different parameters and their physical interpretation is given in Carcione (2001); de la Puente (2008) and figs 2 and 3 in Gregor *et al.* (2022) illustrate all material parameters.

In the following, we will use the Gassmann equivalent (Gassmann 1951; Carcione 2015) to compare the poroelastic model with an elastic approximation. Poroelastic media exist in two states: drained (dry) or undrained (wet). In the drained case, the pore space is empty, and there is no interaction with a fluid phase. This material behaves purely elastically and can be characterized by the Lamé parameters of the matrix λ_M and μ_M together with its density $(1-\phi)\cdot\rho_S$. In the undrained case, the pore space is fluid-filled, and the interaction between both phases changes the physical behaviour. The Gassmann equivalent is an elastic approximation of the undrained poroelastic material. It is described by the density $\phi\cdot\rho_F+(1-\phi)\cdot\rho_S$, the shear modulus $\mu_G=\mu_M$ and the bulk modulus

$$K_G = K_M + \frac{(1-K_M/K_S)^2}{\phi/K_F+(1-\phi)/K_S-K_M/K_S^2} \tag{2}$$

with the matrix bulk modulus $K_M=\lambda_M+\frac{2}{3}\mu_M$. The Gassmann equivalent material reproduces the primary P-wave speed of the undrained poroelastic medium at low frequencies but remains an approximation, as it does not capture wave attenuation, dispersion, or the existence of slow P waves. Because of interactions between solid and fluid phases, the poroelastic material attenuates seismic waves. Moreover, because the fluid phase is not present in the Gassmann equivalent material, it only models the effective stress and does not account the ratio between solid stresses σ and the pressure p. Consequently, the slow P wave is not present in the Gassmann equivalent medium.

During an earthquake, accumulated stresses are suddenly released in the form of slip along a fault. In a dynamic rupture model, the slip evolution along the fault is not prescribed but develops spontaneously. These simulations require initial conditions–the distribution of initial stresses and the parameters of the frictional constitutive law, which can vary across the fault–in solving the equation of motion together with a frictional, internal boundary condition (Harris *et al.* 2018; Ramos *et al.* 2022). Earthquake dynamic rupture models are physically self-consistent. However, they are also computationally expensive (Uphoff *et al.* 2017). They are useful for studying the physics of earthquakes and seismic ground motions, for example, to study topography effects and the influence of the subsurface velocity model on ground motions (Ely *et al.* 2010), to investigate the potential role of seamounts during the 2011 M_w 9.0 Tohoku, Japan earthquake (Duan 2012), to constrain dynamically plausible rupture propagation along a complex system of faults as during the 2016 M_w 7.8 Kaikoura, New Zealand earthquake (Ulrich *et al.* 2019), or to study unexpected ruptures across multiple fault segments during the 2023 M_w 7.8 and 7.7 Kahramanmaras, Turkey earthquake doublet (Gabriel *et al.* 2023).

In our framework, we consider the following fault friction model. The stress field σ along the fault can be decomposed into the normal stress component σ_n and the fault-parallel traction $\vec{\sigma}_t$. The fault strength is computed as $\tau=\mu_\mathrm{f}\cdot\sigma_n$, where μ_f is a dimensionless friction coefficient. If the traction is smaller than the fault strength ($\|\vec{\sigma}_t\|<\tau$), the fault remains locked. If the traction exceeds the fault strength, the fault starts to slide. We adopt the convention that the slip rate vector $\vec{s}$ (i.e. the discontinuity in particle velocity across the fault) is parallel to the fault traction: $\vec{s}\tau=\vec{\sigma}_t\|\vec{s}\|$. The effective friction coefficient μ_f is not constant but can vary in time according to the adopted friction law.

In this study, we consider a linear slip-weakening friction law (Andrews 1976). With increasing slip path length φ, the friction coefficient drops linearly from the static value μ_s to the dynamic value μ_d. Co-seismic weakening occurs over the critical slip distance D_c:

$$\begin{aligned}\mu_\mathrm{f}(t) &= \max\left(\mu_\mathrm{s}-(\mu_\mathrm{s}-\mu_\mathrm{d})\cdot\varphi(t)/D_\mathrm{c},\,\mu_\mathrm{d}\right),\\ \varphi(t) &= \int_0^t \|\vec{s}(\xi)\|\mathrm{d}\xi\,.\end{aligned} \tag{3}$$

2.2 Numerical discretization

Eq. (1) is numerically solved using the ADER-DG implementation by Wolf *et al.* (2022). In this section, we will summarize the key aspects of the discretization: The DG method together with an upwind flux for the spatial discretization as well as the ADER time stepping scheme. Furthermore, we present the key attributes of our incorporation of dynamic rupture sources into ADER-DG scheme.

We discretize the computational domain Ω into a set of non-overlapping and conforming tetrahedral grid cells E_i. Following a Discontinuous Galerkin approach, in each cell, the unknowns $Q_p(t,x,y,z)$ are expanded using a set of polynomials $Q_p(t,x,y,z)=\widehat{Q}_{pl}(t)\Psi_l(x,y,z)$, without requesting continuity across elements. The (solely space-dependent) polynomials Ψ_l are defined locally in each cell. The $\widehat{Q}_{pl}$ denote the time-dependent degrees of freedom. We formulate the finite-element-typical weak form, that is, multiply eq. (1) with a test function, and integrate by parts to obtain

$$\begin{aligned}&\frac{\partial\widehat{Q}_{pl}}{\partial t}\int_{E_i}\Psi_l\Psi_k\mathrm{d}V\\ &-A_{pq}\widehat{Q}_{ql}\int_{E_i}\Psi_l\frac{\partial\Psi_k}{\partial x}\mathrm{d}V-B_{pq}\widehat{Q}_{ql}\int_{E_i}\Psi_l\frac{\partial\Psi_k}{\partial y}\mathrm{d}V\\ &-C_{pq}\widehat{Q}_{ql}\int_{E_i}\Psi_l\frac{\partial\Psi_k}{\partial z}\mathrm{d}V\\ &+\int_{\partial E_i}F_p(\vec{Q}^-,\vec{Q}^+)\Psi_k\mathrm{d}S=\widehat{Q}_{ql}\int_{E_i}E_{pq}\Psi_l\Psi_k dV\,.\end{aligned} \tag{4}$$

In the surface-integral over ∂E_i, the term F then denotes the flux of quantities across the cell boundaries. A suitable numerical flux $F(\vec{Q}^-,\vec{Q}^+)$, which takes the discontinuity between the solution on the interior $\vec{Q}^-$ and the solution on the neighbouring element $\vec{Q}^+$ into account, is crucial for the convergence of the scheme (LeVeque 2002; Hesthaven & Warburton 2008). The purpose of the numerical flux is to approximate the flow of quantities across the interface. We use the upwind-type Godunov flux (e.g. LeVeque 2002) because it is relatively easy to compute and has favourable approximation properties. The Godunov flux solves the Riemann problem, with the quantities $\vec{Q}^+$ and $\vec{Q}^-$ on both sides of the interface as the initial condition, to first compute the state $\vec{Q}^*$ at the interface and then the resulting flux: $F_p(\vec{Q}^-,\vec{Q}^+)=\tilde{A}_{pq}Q^*_q$. Here, $\tilde{A}=n_1A+n_2B+n_3C$ is the matrix describing the flux in the direction of the outward pointing normal $\vec{n}$.

The basis functions Ψ are defined by a set of polynomials on the reference element E_ref. Hence, all integrals involving the basis functions can be pre-computed, which leads to a quadrature-free semi-discrete formulation. For a detailed derivation of the DG discretization of the elastic wave equation, see (e.g. Dumbser & Käser 2006).

The discretization in eq. (4) transforms the system of partial differential equations (PDEs) from eq. (1) into a system of ordinary differential equations (ODEs). Thus, in addition to the DG discretization, we require a time stepping scheme. We employ Arbitrary high-order DERivative (ADER) time stepping, a predictor-corrector scheme (Dumbser *et al.* 2008; Gassner *et al.* 2011), leading to the same convergence order in space and time. First, an element-local predictor is computed. Based on the predictor values, the numerical flux across element interfaces is computed. In the corrector phase, the numerical fluxes are used to obtain the final solution at the next time step. The ADER-DG scheme achieves the same order of convergence in space and time.

Since the coupling between solid and fluid introduces a stiff source term, we need a locally implicit time-stepping scheme, such as the space–time variant of ADER-DG (e.g. Gassner *et al.* 2011), which computes the predictor values from an element-local space–time discretization. de la Puente *et al.* (2008) demonstrated how the stiff source term in the poroelastic wave equation can successfully be integrated using such a space–time ADER-DG scheme. This requires the solution of a linear system with several hundred unknowns for *each* element update. Recently, Wolf *et al.* (2022) derived a more efficient approach based on a blockwise back substitution algorithm. We refer to this previous work for verification of the scheme and description of its parallelization and optimization for current supercomputers.

Dynamic rupture (DR) models simulate the interplay between frictional failure along fault planes with the emanated seismic wave field. In the context of the ADER-DG discretization for elastic and visco-elastic media, the DR source mechanism can be implemented using numerical fluxes (de la Puente *et al.* 2009; Pelties *et al.* 2012a). First, the state $\vec{Q}^*$ at the interface is computed by solving the Riemann problem, just as in the regular case. The state $\vec{Q}^*$ is used to evaluate the normal stress and traction at the fault interface. Based on these quantities, we can evaluate the slip rate s across the face (which might be zero if the fault is still locked). With the slip rate present, an imposed state $\vec{Q}^{\mathrm{DR}}$ is computed, which is consistent with the Rankine–Hugoniot jump conditions in the Riemann problem and the friction law. Then, we use $F_p(\vec{Q}^-, \vec{Q}^+) = \tilde{A}_{pq} Q_q^{\mathrm{DR}}$. More details can be found in (Uphoff 2020; Duru *et al.* 2021).

Finally, we summarize the main steps of our implementation of dynamic rupture sources in poroelastic media, for which the pressure-weakening effect has to be taken into account (more details of the derivation can be found in Appendix B). Again, the state $\vec{Q}^*$ at the interface has to be found, which is the solution to the Riemann problem at the interface. The solution to the poroelastic Riemann problem has to comply with three wave modes: the fast P wave, the S wave, and the slow P wave (Plona 1980). It can be obtained using the Rankine–Hugoniot relations: In the elastic case, the normal stress at the interface σ_n and the traction σ_t are independent of each other. In the poroelastic case, we also have to consider the pressure p^* at the interface, which is tightly coupled to the normal stress (see also Section 3.2). Once the normal stress and the pressure at the interface are available, we consider the effective normal stress $\tilde{\sigma}_n = \sigma_n - p^*$, instead of the normal stress σ_n.

3 RESULTS

In this section, we present simulation results that demonstrate the capabilities of our SeisSol implementation for poroelastic media. First, we verify the correctness of our scheme for double-couple point sources using simple canonical models (homogeneous full space model and a layer-over-half-space model). Then, we demonstrate the geometric flexibility of the tetrahedral meshing on a realistic model of a carbon capture and storage site, which features a complicated layered structure. Finally, we utilize SeisSol to analyse dynamic rupture propagation on branching faults in poroelastic medium and on a planar fault surrounded by a poroelastic fault zone.

Table 1. Material parameters for the double-couple point source in a poroelastic homogeneous full space scenario. The parameters in this table refer to the viscous case. For the inviscid case, consider $\nu = 0$ Pa s. See Section 2.1 for a description of the parameters.

Parameter	Description	Value	
ρ_S	Solid density	2.08×10^3	kg m^{-3}
K_S	Solid bulk modulus	2.0×10^{10}	Pa
λ_M	Matrix 1^{st} Lamé parameter	5.28×10^9	Pa
μ_M	Matrix 2^{nd} Lamé parameter	6.40×10^9	Pa
κ	Matrix permeability	6.00×10^{-13}	m^2
T	Matrix tortuosity	2	
ϕ	Matrix porosity	0.4	
ρ_F	Fluid density	1.04×10^3	kg m^{-3}
K_F	Fluid bulk modulus	2.50×10^9	Pa
ν	Fluid viscosity	1.0×10^{-3}	Pa s

3.1 Seismic waves radiated by a double-couple point source in poroelastic media

3.1.1 Verification of the double-couple implementation in a poroelastic homogeneous full space model

If we are interested in seismic waves at teleseismic distances from the hypocentre, the slip at the fault may be approximated by a dislocation at an infinitesimally small fault, that is, as slip at a point. The seismic wave field radiated by earthquakes can be approximated by the wave field radiated by a double-couple (DC) point source (Aki & Richards 2002). A DC source may be described by a moment tensor M. Wolf *et al.* (2022) used an explosive point source to verify the ADER-DG scheme for poroelastic media in the open-source software SeisSol. However, the explosive source radiates P waves only. Therefore, here, we first verify the scheme using a DC point source that radiates both P and S waves.

We consider a model of a homogeneous full space similar to that of Wolf *et al.* (2022), but replace the explosive source with a DC point source. We use the definition of the fault coordinate systems as by Moczo *et al.* (2014), and consider a source located at the origin with $\Phi_s = \delta = \lambda = 0.0\,^\circ$, corresponding to $M_{xz} = M_{zx} = -1$ being the only non-zero components of the moment tensor. The source time function is a Ricker wavelet with dominant frequency $f_0 = 16$ Hz and time delay $t_0 = 0.07$ s. We study two different materials, which only differ in their fluid viscosity. The material parameters (including viscosity ν for a viscous fluid) are given in Table 1. Additionally, we consider an inviscid fluid with viscosity $\nu = 0.0$ Pa s. We place 12 receivers in the x–z-plane along three different diagonals at angles $0\,^\circ$, $22.5\,^\circ$ and $45\,^\circ$ from the x-axis, at distances 600, 1000, 1800 m or 3000 m from the source, respectively, as illustrated in Fig. 1.

The 3-D mesh spans the volume $[-7\,\mathrm{km}, -7\,\mathrm{km}]^3$, centred around the origin. Within a cuboid around the receivers and the source, we specify a characteristic mesh size of 30.0 m. The refinement area is rotated with respect to the domain boundaries such that it symmetrically aligns with the receiver locations (Fig. 1).

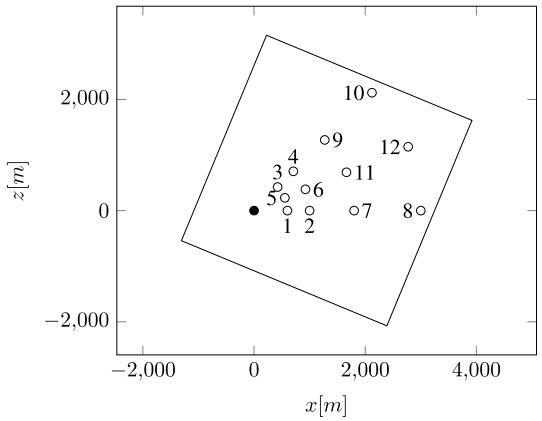

Figure 1. Receiver positions for the double-couple (DC) point source 3-D scenario in the x–z-plane. All receivers are located either 600, 1000, 1800 m or 3000 m away from the source at 0°, 22.5° and 45° from the x-axis, respectively. The filled black circle indicates the DC source location. The black rectangle shows the area in which the mesh is adaptively refined.

Within a sphere of radius 20 m, we locally refine the mesh down to a characteristic edge length of 3 m. Towards the boundary, the characteristic mesh size grows up to 240 m. This mesh refinement strategy is chosen to balance the resolution of waves in the area of interest and the computational cost. In total, the mesh consists of 47 200 000 tetrahedrons. We use fifth degree polynomials, resulting in a convergence order of $O6$. We computed the numerical solution using 300 nodes of the supercomputer SuperMUC-NG installed at the Leibniz Supercomputing Centre (LRZ). The reference solution is computed using the semi-analytical solution of Karpfinger *et al.* (2009).

Fig. 2 shows a detailed comparison of particle velocity u calculated using SeisSol and the reference solution at a selected receiver 10. To assess the accuracy, we evaluate envelope misfit (EM) and phase misfit (PM) following Kristekova *et al.* (2006, 2009). The EM quantifies differences between two signals whereas PM quantifies differences in phase. Low EM and PM indicate very good agreement between the solutions for the inviscid as well as the viscous fluid model setups. We note that the misfits are slightly higher when using the inviscid fluid. In the inviscid case, the slow P wave is propagating with lower velocity and thus has a shorter wavelength, which renders this case numerically more challenging.

To evaluate the overall accuracy, we show EM and PM values for all three components of particle velocity and relative fluid velocity at all receivers in Fig. 3. The EM and PM values of u, w, u_f and w_f are also tabulated in the Appendix (Tables D1 and D2).

First, let us explain the origin of the rather large EM and PM misfits of up to 8 and 2.5 per cent, respectively, characterizing the relative fluid velocities at receivers 9 to 12. In the inviscid case, the slow P wave is propagating with a wavelength of 26.4 m at 40 Hz, which approximately matches the maximum frequency of the source time function. The affected receivers are located at a distance of 1800 m or 3000 m, corresponding to several tens of wavelengths of the slow P wave. The numerical convergence analysis in Käser *et al.* (2008) suggests that using two elements per wavelength is required for fifth degree polynomial basis functions in the ADER-DG method to achieve sufficiently accurate results. Thus, to accurately simulate the propagation of the slow P wave, we would need a mesh with an element size of 13.25 m. With an element size of 30 m, the numerical solution for the slow P wave is underresolved. We note that we do not observe large EM and PM values at receivers 7 to 8. These are at the same distances from the source as receivers 9 to 12, but owing to the source orientation, they fall in the direction of pure S-wave radiation. Thus, there is no slow P wave propagating in the direction of receivers 7 to 8, and consequently, the EM and PM misfits are not affected by the underresolved slow P wave. We did not rerun the simulation with finer resolution because this issue only affects the slow P wave in the unrealistic inviscid case. Moreover, as can be seen from Fig. 2, only relative fluid velocities are affected significantly, but these are challenging to measure observationally. Nevertheless, we included the non-converged cases in Fig. 3 for completeness, but using different symbols (open circles).

In summary, we observe a very good agreement between the (converged) SeisSol results and the reference solutions, with EM below 2 per cent and PM below 0.5 per cent.

3.1.2 *Verification of the double-couple implementation in a poroelastic layer-over-half-space model*

We verified the homogeneous full-space model solution (in Section 3.1.1) against a semi-analytical reference solution. However, such a semi-analytical solution is not applicable to a model with internal interfaces or a free surface. Both present important features for realistic numerical simulations of seismic wave propagation in poroelastic materials. Therefore, we next verify our poroelastic ADER-DG scheme in a layer-over-half-space, model which contains one internal interface and a planar, free surface. Since we are not aware of available (semi-)analytic solutions, we compare our ADER-DG solution with a solution obtained by the finite-difference method (Moczo *et al.* 2019; Gregor *et al.* 2021, 2022).

We parametrize a poroelastic layer over a poroelastic half-space, similar to the 'LOHp' model of Wolf *et al.* (2022). The layer is 500 m thick and consists of a softer material with slower wave speeds compared to the half-space. Atop the slower layer, we impose a free-surface boundary condition. The material parameters for the layer and the half-space are given in Table 2. We specify a DC source with $\Phi_s = 90°$, $\delta = 22.5°$ and $\lambda = 90°$. Since the slip vector lies in the $x - z$ plane, it allows the creation of a line source by extending the source along the y-axis to enable comparison of the results with a 2-D finite-difference solution. We place the source at depth $z = 1010$ m. We use a Gabor wavelet with a flat spectrum up to roughly 10 Hz as the source time function

$$s(t) = \cos(\omega(t - t_0)) \cdot \exp(-(\omega(t - t_0)/\gamma)^2)\,, \tag{5}$$

where $\omega = 2 \cdot \pi \cdot f_0$ and $f_0 = 0.5$, $\gamma = 0.25$, $t_0 = 0.25$.

We create an unstructured tetrahedral mesh of the domain spanning $[-10\,\mathrm{km}, 10\,\mathrm{km}] \times [-10\,\mathrm{km}, 10\,\mathrm{km}] \times [-7\,\mathrm{km}, 0\,\mathrm{km}]$. The layer interface at 500 m depth is explicitly meshed. At the top, we impose a free surface boundary condition, while for all other five boundaries, we impose absorbing boundaries to mimic an unbounded half-space. Utilizing the flexibility of an unstructured tetrahedral mesh, we use different element-size constraints in different parts of the mesh, reflecting different requirements on the local accuracy. Such an unstructured mesh allows achieving high accuracy while also maintaining high efficiency. The desired element edge length during the mesh generation is set to 50 m in the cuboid $[-500\,\mathrm{m}, 2500\,\mathrm{m}] \times [-1500\,\mathrm{m}, 1500\,\mathrm{m}] \times [-1500\,\mathrm{m}, 0\,\mathrm{m}]$ and coarsened towards the boundary to up to 250 m. In addition, we refine the mesh towards the source to a high resolution of up to 10 m element edge length. To capture the slow P-wave accurately, we further refine the mesh inside the layer and below the interface up to a resolution of 5 m (i.e. in the region

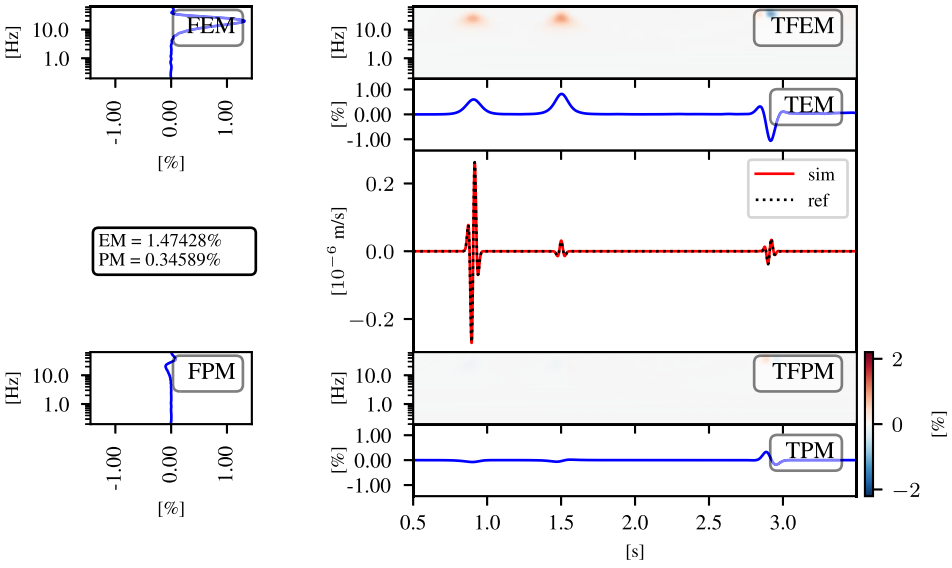

(a) Pores filled with an inviscid fluid.

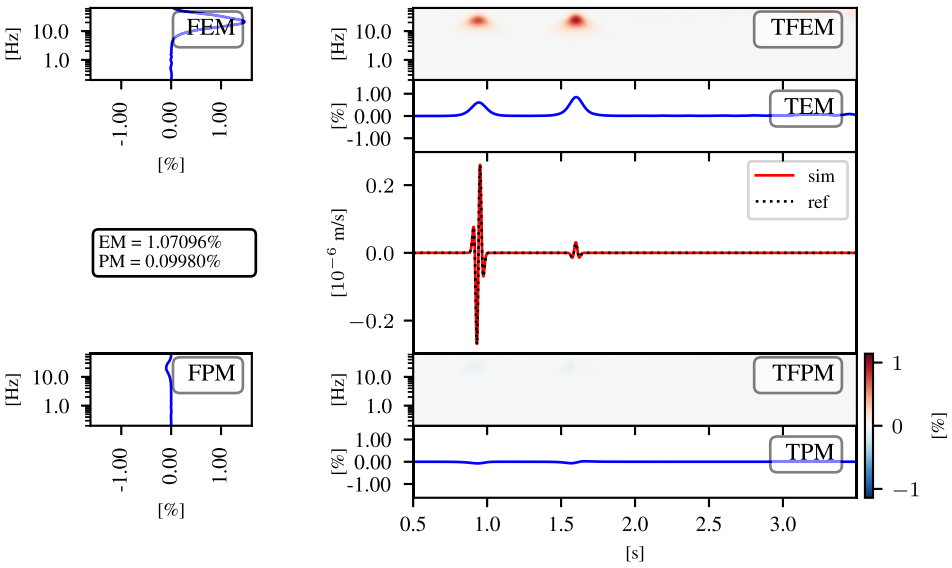

(b) Pores filled with a viscous fluid.

Figure 2. Detailed time-frequency misfit plots for the particle velocity u at receiver 10 in the homogeneous full space test case. The plots show the difference between the numerical SeisSol solution ("sim", in red) and the semi-analytical reference solution ("ref", black dots). We plot several time-frequency misfit criteria (Kristekova *et al.* 2006, 2009): Frequency Envelope Misfit (FEM), Time-Frequency Envelope Misfit (TFEM), Time Envelope Misfit (TEM), single-valued Envelope Misfit (EM), single-valued Phase Misfit (PM), Frequency-Phase Misfit (FPM), Time-Frequency Phase Misfit (TFPM) and Time-Phase Misfit (TPM).

$[-200\,\text{m}, 2200\,\text{m}] \times [-500\,\text{m}, 500\,\text{m}] \times [-550\,\text{m}, 0\,\text{m}]$). The line source is represented by point sources equally spaced with 50 m distance along the y-axis. The mesh contains 47 500 000 tetrahedrons. As before, we use polynomials up to degree 5 as basis functions, to achieve a convergence order of $O6$. The total simulation time is 2 s. The reference finite difference (FD) solution is computed on a regular uniform grid with 0.625 m grid spacing.

We record the wave field at a set of receivers placed along a regular grid with lateral distances of 0, 250, 500 and 1000 m from the source. The complete receiver configuration is depicted in Fig. 4: We place the receivers with a spacing of 5 m between depths of 5 and 35 m. To enable a more accurate analysis of the seismic wave field near the free surface, we specify additional receivers at a depth of 0.5 and 2.5 m. We also place receivers in the middle of the layer, above and below the interface, and in the half-space. We do not consider receivers directly at the free surface because, in the FD method, the free-surface boundary condition ($p \equiv 0$) is enforced exactly, whereas, in the DG framework, the free-surface boundary condition is only enforced in a weak sense by imposing a particular flux term. Consequently, pore pressure

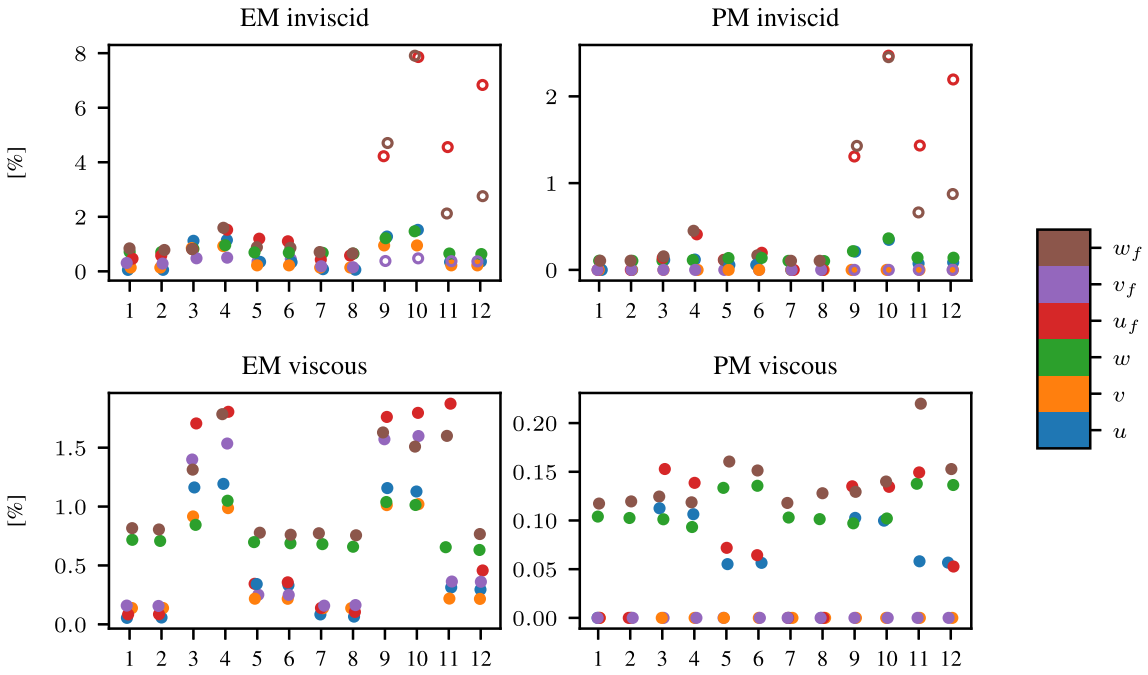

Figure 3. Envelope misfits (EM) and phase misfits (PM) for different quantities (indicated by colours) at all receivers (indicated by numbers at x-axis) in the poroelastic homogeneous full space model setup. Note: The open circles denote non-converged solution components. See the text for a more detailed explanation.

Table 2. Material parameters for the poroelastic layer-over-half-space scenario.

Parameter	Halfspace	Layer	
ρ_S	2.50×10^3	2.21×10^3	kg m^{-3}
K_S	40.0×10^9	7.60×10^9	Pa
λ_M	12.0×10^9	3.96×10^9	Pa
μ_M	12.0×10^9	3.96×10^9	Pa
κ	6.00×10^{-12}	1.00×10^{-12}	m^2
T	2	2	
ϕ	0.20	0.16	
ρ_F	1.04×10^3	1.04×10^3	kg m^{-3}
K_F	2.5×10^9	2.5×10^9	Pa
ν	1.0×10^{-3}	1.0×10^{-3}	Pa s

at the free surface in DG solutions will be small but not obey to $p \equiv 0$. Quantifying the (mis)match between the solutions using a relative error measure (such as the time-frequency misfits) when the reference solution is exactly zero would lead to misleading results.

Above, in Section 3.1.1, we have compared the solid velocities and the relative fluid velocities with the reference solution. The relative fluid velocities are important auxiliary quantities for the numerical method and are therefore important for comparing the results of two numerical methods. However, because they quantify the relative motion of the fluid in the pore space with respect to the motion of the matrix, they can hardly be observed in reality. In the previous section, we have concentrated on the relative fluid velocities. The analytic reference solution only provided the displacement of the matrix together with the relative fluid motion. The more relevant quantity with practical implications is the fluid pressure. Consequently, we will focus on the evaluation of solid velocities and fluid pressure from now on.

Fig. 5 summarizes the envelope misfits for x- and z-components of particle velocities, u and w, and pore fluid pressure p. If we consider the receivers at 2.50 m depth and below, we find that the envelope misfits are well below 3 per cent. For the near-surface receivers (depth of 0.5 m), we observe very small envelope misfits (EM) for particle velocities, consistently with the small EM values for deeper receivers. However, for pore pressure, we observe much larger EM values up to 2 per cent with one outlier at 2.5 per cent. We suspect that the receiver at $x = 500$ m, $z = -15$ m is within or close to a tetrahedron with a non-optimal shape, that is, a skewed aspect ratio. Since meshing for this scenario was already challenging, and a misfit of 2.5 per cent at a single point does not question the quality of the overall results, we decided to keep the mesh as it is and refrain from further refinement. All phase misfits are well below 1.5 per cent.

To explain the partially elevated EM values, let's have a closer look at the depth-dependent evolution of pore pressure near the free surface. Fig. 6 shows the pore pressure time histories at $x = 1000$ m recorded at different receiver depths. First, we see that the pore pressure at the free surface (blue line) is visually zero, as expected and explained above. Second, the magnitude of pore pressure does not significantly vary for depths between 2.5 and 30 m. This implies that the transition of pore pressure from 0 Pa at the free surface to ~ 30 Pa must occur within the top 2.5 m. Capturing such steep variations of pore pressure is inherently challenging for elements with an edge length of 5 m. We recall that the reference FD solution is obtained with a grid spacing of 0.625 m. From Fig. 5, we can conclude that the overall agreement is good. However, if high accuracy in modelled pore pressure near the free surface is important, the use of even smaller element sizes is inevitable.

Fig. 7 shows the distribution of pore pressure for the poroelastic layer-over-half-space model. Due to the steep increase of pore pressure near the free surface (depicted in Fig. 6), we cannot see zero pore pressure at the free surface (the top edge of the plot). We also observe an apparent discontinuity in pore pressure at the internal interface. The explanation of this effect is similar to that of the free-surface effect. Pore pressure variations near the internal interface are too steep to be captured at this scale.

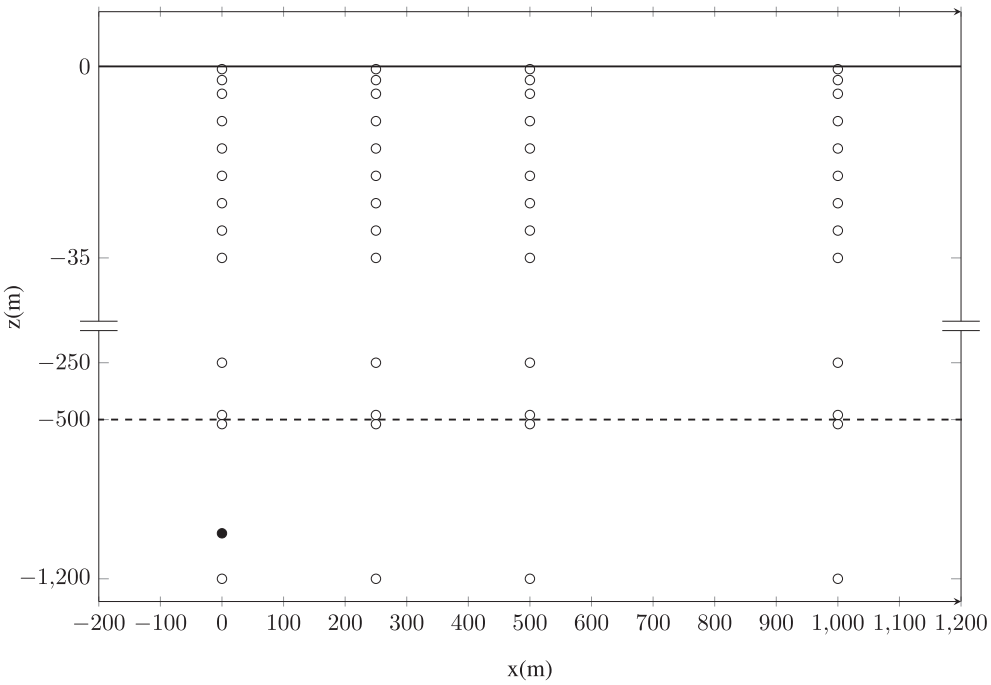

Figure 4. Receiver positions (circles) for the poroelastic layer-over-halfspace scenario. The thick black line at $z = 0$ m represents the location of the free surface, and the dashed line represents the location of the material interface. The filled black circle denotes the double-couple source position. Note that the z-axis contains a break and uses a zoomed-in scale above the break.

3.1.3 Application to the Sleipner, Utsira, carbon capture and storage site

In this section, we apply SeisSol to model seismic wave propagation in a realistic 3-D poroelastic model of a CCS site, Sleipner, which is a part of the larger Utsira Formation, a deep saline reservoir located 800 to 1000 m below the sea floor off the coast of Norway.

First, we briefly describe the procedure for developing the computational model: We define a complex 3-D geometry of interfaces separating sandstone layers by impermeable shale layers from the Sleipner 2019 benchmark model (Equinor 2019). For a complete characterization of a poroelastic material, we need ten parameters. However, such a detailed description of the materials is not available neither for the Sleipner site nor the Utsira formation. We, therefore, derive the missing material parameters as described in the following: First, we use *P*-wave velocities for the Utsira formation reported by Yan (2017), who further refers to Traub (2008). Based on the *P*-wave speed values, we associate individual layers with one of five poroelastic materials: caprock, sandstone, thick shale, intra-shale and bedrock. Additionally, we consider a roughly 700 m thick, effectively elastic layer above the caprock.

Fig. 8 depicts the overall structure of our model. The *S*-wave speeds are calculated from the respective *P*-wave speeds using empirical relations by Vernik *et al.* (2002) and Mavko *et al.* (2009). These empirical relations distinguish between brine-saturated sandstones and shales. Therefore, we use these relations for the sandstone material and all shale materials (including caprock and bedrock), respectively. Density is determined by the power-law form of Gardener's empirical relation, with coefficients for sandstone (Gardner *et al.* 1974; Castagna & Backus 1993; Mavko *et al.* 2009) consistently with Yan (2017). The estimated values of *P*- and *S*-wave speeds and density are given in Table 3. We use them as the input to our rock physics inversion, which is based on a nearest-neighbour algorithm utilizing Voronoi cell sampling (Sambridge 1999; Dupuy *et al.* 2016).

To better constrain the inversion, we fix values of fluid bulk modulus, fluid density and viscosity, assuming the pore space is filled with brine. To further help constrain the inversion, we also assume *a-priori* values of solid bulk modulus K_S, solid density ρ_S and permeability κ. Yan (2017) provided values of the three parameters for sandstone and bedrock in the Utsira formation, but we assume that all shale layers (thick shale, intra-shales, caprock and bedrock) have the same properties regarding K_S, ρ_S and κ. Since we find that the inversion very poorly constrains tortuosity, we use a fixed value for the tortuosity of all materials in our model. Subsequently, the rock physics inversion is used to find the values of elastic moduli of the matrix and porosity.

SeisSol currently does not support combining elastic and poroelastic materials in one computational simulation. Therefore, instead of parametrizing an elastic layer above the caprock, we use a poroelastic material with negligible poro-elastic effects, that effectively behaves as elastic material. All poroelastic material parameters for all materials in the computational model are summarized in Table 4. Note that except for the sandstone layers, all other layers are almost impermeable.

The thickness of some intra-shale layers in the original model is only 1 to 2 m, which is very small compared to the wavelengths expected in the model for a dominant frequency of 16 Hz (tens of meters). Therefore, to facilitate the meshing process, we modified the original model such that all layers are at least 5 m thick. Since the wavelengths in this scenario are well above 35 m, we do not expect that this changes the results significantly. Furthermore, in this test case, we are not interested in reproducing real-world recordings, therefore this change of geometry does not have a large influence on our results. To avoid intersections of these thicker layers, we also removed some of the intra-shale layers. The area

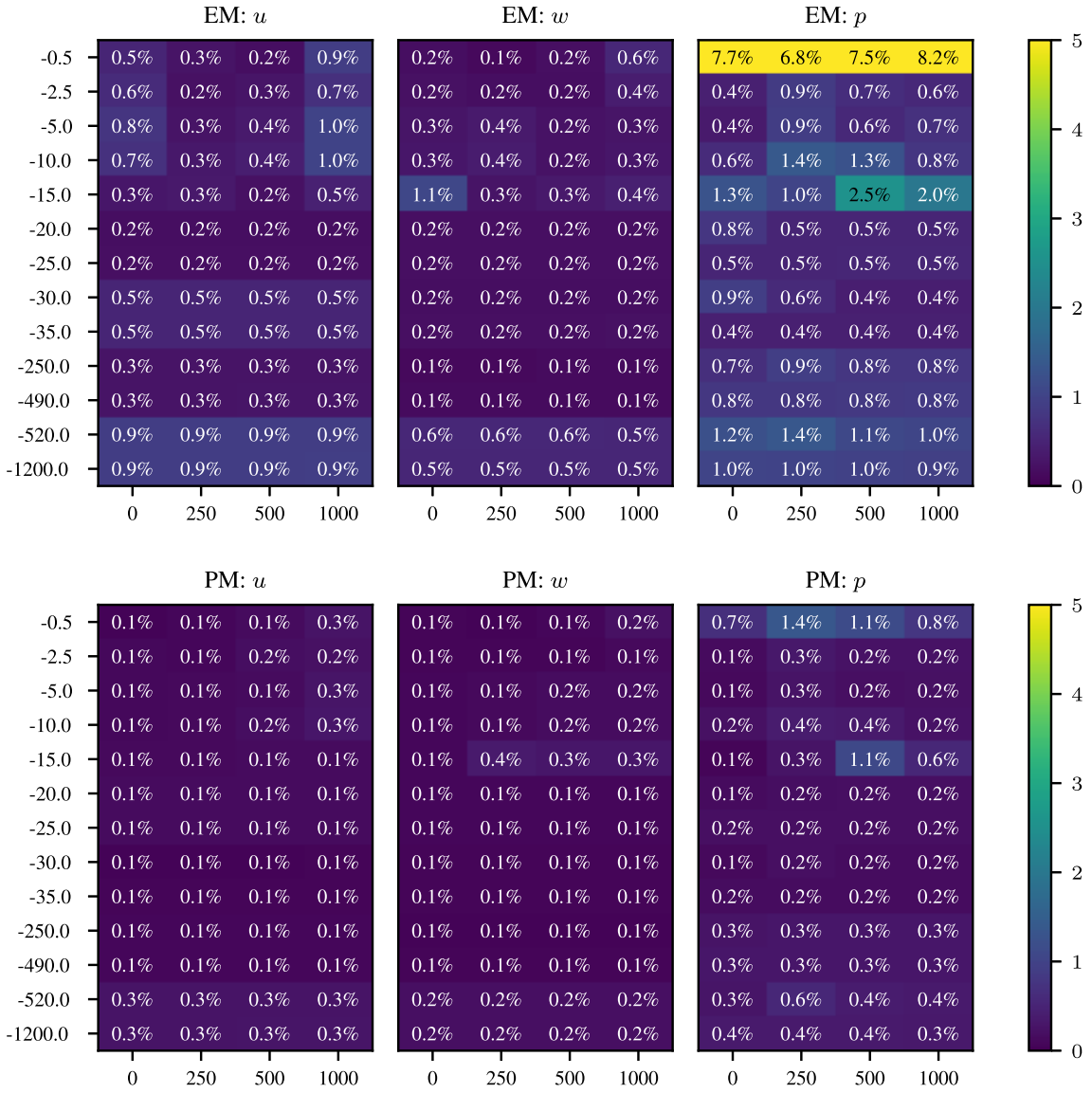

Figure 5. Envelope and Phase misfits between the SeisSol DG solution and the finite difference (FD) reference solution at receiver points in the poroelastic layer-over-half-space model. Compare to Fig. 4 for a sketch of the source–receiver configuration. Except for the pressure close to the free surface, we find excellent agreement between the DG simulation results and the FD reference solution.

of interest, including the complex geometry and interfaces, spans [0 m, 3200 m] × [0 m, 5900 m]. To minimize potential artificial reflections from the absorbing boundaries, we enlarge the mesh to the area [−5000 m, 8000 m] × [−5000 m, 11000 m] and to a depth of 6500 m. We enforce a characteristic edge length of 10 m in the bulk and 5 m in the thinnest layers, resulting in a mesh with 65 000 000 tetrahedrons. Again, polynomials up to degree 5 are used as basis functions.

The geometric flexibility of the DG method allows us to explicitly represent the layer interfaces in the inner mesh, where the 3-D geometry of the layers is available. Outside this area, we infer a 1-D depth-dependent material model. Therefore, we compute the average depth of each interface and enforce a planar interface outside the area, where detailed layer information is available. The characteristic edge length for the tetrahedral mesh generation is set to 5 m in order to align with the thickness of the shale layers. A lower resolution version of the resulting mesh is shown in Fig. 8.

We consider a double-couple point source with $\Phi_s = 90.0^\circ$, $\delta = 90.0^\circ$ and $\lambda = 0.0^\circ$ with its hypocentre at $(x, y, z) = (1500\,, 3000\,, 1500\,\text{m})$. The source time function is a Ricker wavelet with a dominant frequency of $f_0 = 16\,\text{Hz}$, which is identical to the verification setup in the poroelastic homogeneous full-space model. We record the seismic wave field at a line of receivers at $x = 1750\,\text{m}$, $y = 3750\,\text{m}$ and $z = 0\,\text{m}, 5\,\text{m}, \ldots, 2000\,\text{m}$.

We compare the poroelastic version of the model to the elastic equivalent, using the Gassmann approximation (Gassmann 1951; Carcione 2015). Fig. 9 shows the envelope misfits (EM) for solid particle velocities between poroelastic and equivalent elastic models. The EM values remain consistently below 0.5 per cent throughout the domain, which implies that both models essentially yield the same deformation of the matrix. However, this interpretation ignores the effect of pore pressure.

The pressure of pore fluids is only explicitly modelled using the poroelastic model. In the Gassmann equivalent elastic model,

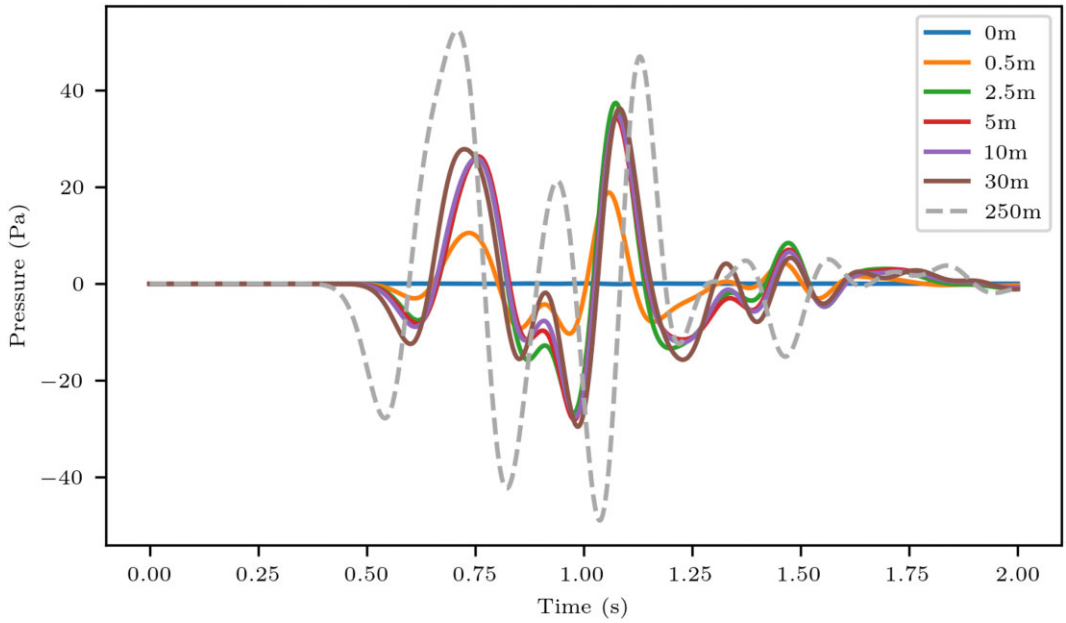

Figure 6. Time history of the pressure at $x = 1000$ m for different receiver depths in the poroelastic layer-over-half-space SeisSol DG simulation. The pressure at $z = 0$ m is zero, reflecting the traction-free boundary condition. Already at a depth of $z = 0.5$ m, we observe a pressure field at roughly half the amplitude compared to a depth of $z = 250$ m. This highlights the steep pressure gradient towards interfaces.

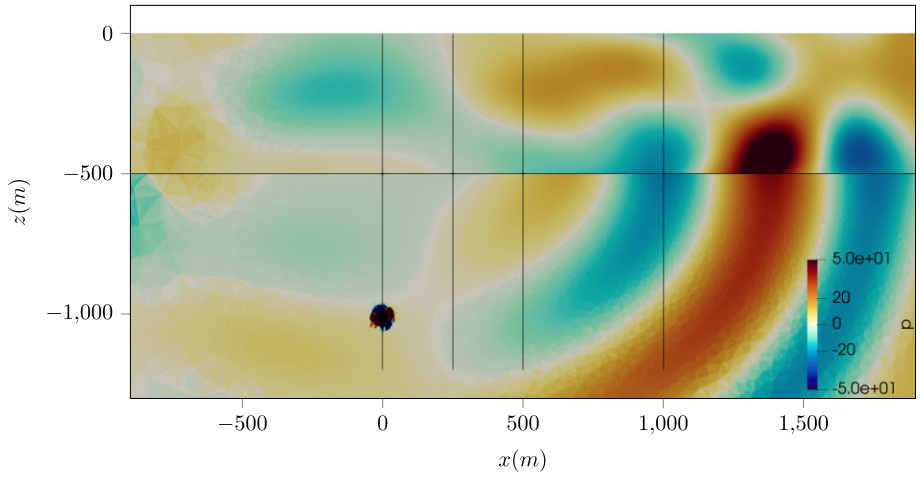

Figure 7. Snapshot of the pressure field at 1.3 s. Black lines denote the lines of receivers at $x = 0$, 250, 500 and 1000 m as well as the interface at 500 m depth. The black circle denotes the position of the DC source. At this scale, the pressure appears to be discontinuous across the interface. See also Fig. 6 for a detailed overview of the pressure field at an interface.

the total stress σ is the sum of the fluid pressure p and the stress sustained by the matrix $\tilde{\sigma}$, but fluid pressure is not readily quantifiable. In the sandstone layers, the fluid pressure can account for up to two-thirds of the total stress. The fault strength depends on the stress sustained by the matrix $\tilde{\sigma}$ only. Thus, the correct computation of the fluid pressure is vital to assess, for example, whether dynamic triggering of an earthquake may occur.

We conclude that for poroelastic seismic wave propagation scenarios where only the displacement of the solid matrix is of interest, the Gassmann equivalent is a sufficient approximation. This includes, for example, ground motion estimates from kinematic earthquake source models. However, in the next section, we will study fault interaction in dynamic rupture earthquake models in poroelastic media, for which the fluid pressure can have a significant impact on the dynamic rupture nucleation, propagation and arrest (e.g. Kammer *et al.* 2024). In these cases, the Gassmann equivalent approximation can lead to misleading conclusions.

3.2 3-D dynamic rupture in poroelastic media

Dynamic rupture models combine frictional failure along the fault and seismic wave propagation in the surrounding rock volume. In this section, we will extend 3-D dynamic rupture simulations with SeisSol to poroelastic materials and present two scenarios in which the incorporation of poroelastic materials significantly changes rupture dynamics. We here study the dynamic effects of poroelasticity in 3-D multifault rupture branching and poroelastic fault zone models, paying special attention to the undrained pore pressure changes and their impact on fault strength and rupture propagation.

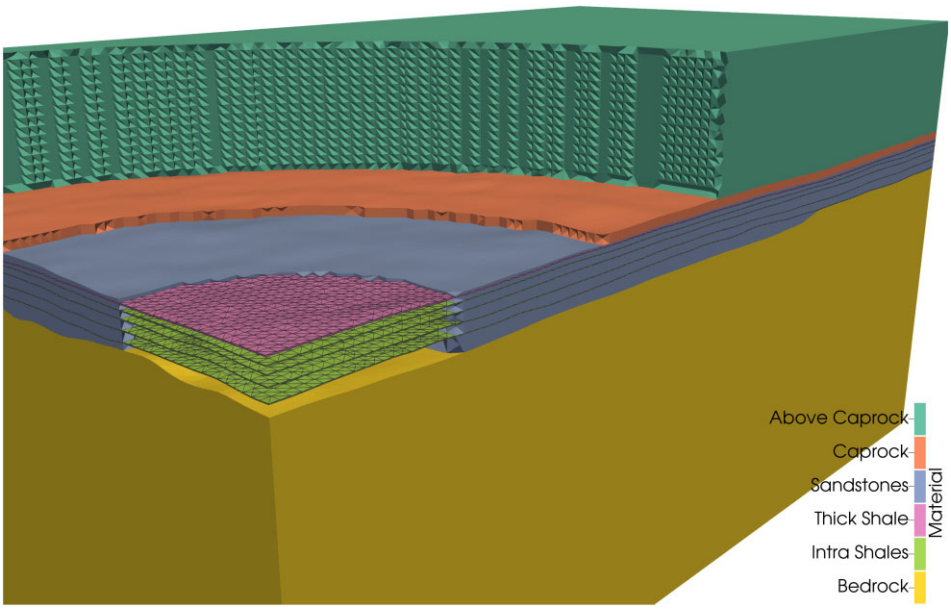

Figure 8. View of the unstructured tetrahedral mesh adapted from the geometrically complex 3-D Sleipner, Utsira CCS site. To clearly illustrate the different layers and how they are geometrically represented in the mesh in this figure, the mesh resolution is lower than for the mesh that is used for the numerical simulations with SeisSol. The mesh shown in this figure contains 6799 000 elements, while the fine mesh used in the simulations contains 6500 000 elements.

Table 3. Estimated *P*-wave speed (V_P), *S*-wave speed (V_S) and density (ρ) for the subsurface materials in the Sleipner, Utsira CCS site model that we use as an input for a rock physics inversion.

Parameter	Above Caprock	Caprock	Sandstones	Thick Shale	Intra Shales	Bedrock	
V_P	1900	2300	2050	2250	2150	2490	$\mathrm{m\,s^{-1}}$
V_S	711	900	589	858	773	1040	$\mathrm{m\,s^{-1}}$
ρ	2080	2060	2000	2050	2030	2230	$\mathrm{kg\,m^{-3}}$

Table 4. Poroelastic material parameters for the modified Sleipner, Utsira CCS site computational model.

Parameter	Above Caprock	Caprock	Sandstones	Thick Shale	Intra Shales	Bedrock	
K_S	37.0×10^9	22.6×10^9	32.3×10^9	22.6×10^9	22.6×10^9	22.6×10^9	Pa
ρ_S	2.02×10^3	2.39×10^3	2.66×10^3	2.39×10^3	2.39×10^3	2.39×10^3	$\mathrm{kg\,m^{-3}}$
λ_M	5.20×10^9	1.89×10^9	2.81×10^9	1.65×10^9	1.21×10^9	2.91×10^9	Pa
μ_M	1.01×10^9	1.67×10^9	0.695×10^9	1.51×10^9	1.21×10^9	2.29×10^9	Pa
κ	1.00×10^{-21}	1.47×10^{-17}	2.00×10^{-12}	1.47×10^{-17}	1.47×10^{-17}	1.47×10^{-17}	$\mathrm{m^2}$
T	3.0	1.0	1.0	1.0	1.0	1.0	
ϕ	0.02	0.24	0.4	0.25	0.27	0.21	
ρ_F	1.2	1.03×10^3	1.03×10^3	1.03×10^3	1.03×10^3	1.03×10^3	$\mathrm{kg\,m^{-3}}$
K_F	101×10^3	2.3×10^9	2.3×10^9	2.3×10^9	2.3×10^9	2.3×10^9	Pa
ν	1.9×10^{-4}	6.9×10^{-4}	6.9×10^{-4}	6.9×10^{-4}	6.9×10^{-4}	6.9×10^{-4}	Pa s

Previous studies have shown that a critical aspect of modelling dynamic fault strength in poroelastic media is determining the fault pore pressure, which directly influences the effective normal stress and consequently the rupture process of sub- and supershear ruptures (Rudnicki & Rice 2006; Dunham & Rice 2008; Jha & Juanes 2014; Song & Rudnicki 2017; Yang & Juanes 2018; Heimisson *et al.* 2021; Li & Zhang 2023; Pampillón *et al.* 2023). Pressure changes across the fault surface depend on the assumed poroelastic parameters and may be discontinuous and antisymmetric, with fluid flow and fault permeability determining the pressure distribution. The short timescales of dynamic rupture simulations account for undrained pore pressure changes, which predominantly affect the effective normal stress. Pore pressure is only uniquely determined when accounting for the continuous fluid flow at the mm-scale in the fault normal direction. However, accurately determining pore pressure on the fault remains challenging, particularly given that small-scale processes such as dilatancy and compaction are not fully constrained at seismogenic depths. Therefore, simplified approaches were considered to account for the pore-pressure effects at the fault. Assuming that the fault is completely impermeable with slip occurring just on one side of the impermeable seal, the fault strength can be determined by using pressure changes on that side. Alternatively, the strength can be determined on both sides of the fault (taking into account pore-pressure on each side) and the fault strength is then selected as the weaker strength. Another approach is to average the pore-pressure values at each side of the fault and then determine the fault strength. However, these simplified approaches lead to radically different predictions on rupture dynamics.

Dynamic rupture models have been implemented in various computational methods that have been established to solve the elastic

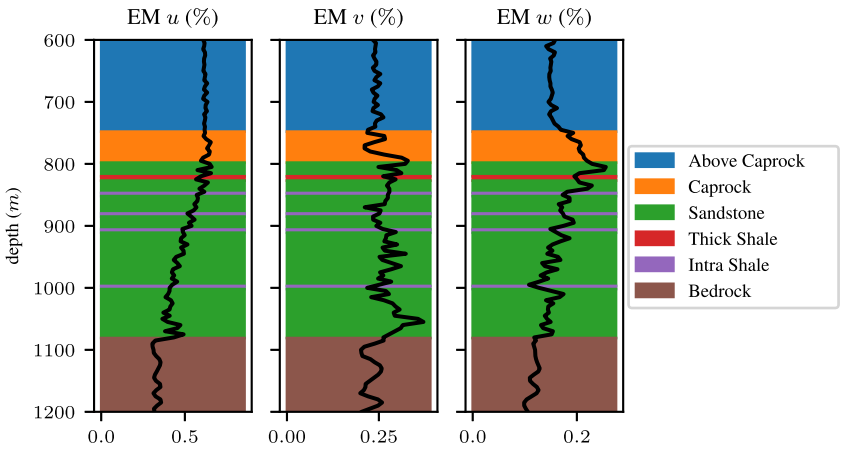

Figure 9. Comparison of the displacement of the elastic matrix between the true poroelastic material and the Gassmann equivalent in the Seipner, Utsira CCS site SeisSol simulations. For all three velocity components, we compute the envelope misfit for receivers placed at $x = 1750$ m, $y = 3750$ m with a vertical distance of 5 m. We focus on the sandstone-shale formation between 600 and 1200 m depth. With misfits well below 1 per cent, we conclude that the true poroelastic material and the Gassmann equivalent yield similar results.

wave equations, including Finite Differences, Finite Elements, Finite Volumes, Discontinuous Galerkin (DG) and Boundary Integral methods (e.g. Day 1982; Cruz-Atienza & Virieux 2004; Day *et al.* 2005; Barall 2009; Ely *et al.* 2009; Aagaard *et al.* 2013; Zhang *et al.* 2014; Uphoff 2020). For dynamic rupture simulations using the ADER-DG approach, a Riemann problem is solved to obtain the traction and velocity values at the fault interface (de la Puente *et al.* 2008; Pelties *et al.* 2012b; Duru *et al.* 2021). Then, the slip rate is computed to be consistent with the friction law and the surrounding elastodynamic wave field. Based on the slip rate, an imposed state at the interface is calculated, which is used in the flux computation later on. In order to combine poroelastic media and dynamic rupture, the solver for the Riemann problem needs to be adapted to take the fluid pressure into account. When the fluid pressure p and the stress in normal direction σ_n at the fault are known, we can compute the effective stress as $\tilde{\sigma} = \sigma_n - p$ (see Section 2.2). In our model, we choose the fluid pressure p to be the average of the fluid pressure on both sides of the fault.

3.2.1 3-D rupture dynamics across branching faults in poroelastic materials

We examine how poroelastic materials influence dynamic rupture across a branching multifault geometry. We consider a homogeneous half-space with a vertical planar fault. The main fault is defined as the plane $[-16000\,\text{m}, 12000\,\text{m}] \times \{0\} \times [-15000\,\text{m}, 0\,\text{m}]$. At $x = 0$, the branch segment intersects the main fault. The branch has the same width as the main fault and is 12 km long. The angle between the branch and the main fault is 15 °. The resulting fault geometry is depicted in Fig. 10.

This 3-D model setup is similar to the TPV24 scenario (Harris *et al.* 2009), but the branching angle has been reduced, and the branch is located on the other side of the main fault. We modified the original TPV24 benchmark scenario to investigate the weakening effect of the fluid pressure. In the original configuration, the branch is located in a region of reduced pore-fluid pressure induced by the propagating rupture, thus inhibiting further rupture propagation on the branch. In our modification, the branch is located in the region of increased pore-fluid pressure, allowing us to investigate whether increased pore pressure facilitates dynamic rupture propagation. We performed several trial-and-error simulations with varying branching angles. We chose the scenario with the most pronounced effect of poroelastic rheology.

We consider a uniform background stress tensor

$$\sigma = \begin{pmatrix} -17.0 \times 10^7 & 4.5 \times 10^6 & 0.0 \\ 4.5 \times 10^6 & -1.00 \times 10^7 & 0.0 \\ 0.0 & 0.0 & -1.00 \times 10^7 \end{pmatrix} \text{Pa} \tag{6}$$

and employ linear slip weakening friction with $\mu_s = 0.7$, $\mu_d = 0.3$, $D_c = 0.1\,m$. These friction parameters differ from the original description of TPV24. In particular, D_c is chosen smaller, as 0.1 m. In this section, we will conduct a parameter study comparing several poroelastic materials. In order to nucleate rupture with uniform fault parameters in all of considered materials, we decided to use this smaller value of D_c. To suppress supershear transition at the free surface, we set the cohesion at the free surface to $C = 1$ MPa, which linearly decreases to 0 at a depth of 1000 m. Below, the cohesion is 0. We initiate the rupture by prescribing local fluid overpressure lowering the effective normal stress:

$$p_0 = \exp\left(-1 \times 10^{-6}\left((x + 8000)^2 + (y + 500)^2 + (z + 10000)^2\right)\right) \cdot 8.0\,\text{MPa}. \tag{7}$$

The Gaussian distribution corresponds to pore pressure distribution from an instantaneous pressure point source (Shapiro 2015). Although there are more realistic models of pore pressure distribution due to fluid injection (e.g Shapiro 2015; Galis *et al.* 2017), the Gaussian perturbation is sufficient for our case.

We consider the material parameters used by Pampillón *et al.* (2023) (Table S2 in Supporting Information), see Table 5. The *SeisSol* parameters can be obtained using these relations: $\mu_M = \frac{E}{2(1+\nu_P)}$, $\lambda_M = \frac{E \cdot \nu_P}{(1+\nu_P)\cdot(1-2\nu_P)}$, $K_M = \lambda_M + \frac{2}{3}\mu_M$, $K_S = \frac{K_M}{1-\alpha_B}$, and $K_F = \frac{1}{\beta}$.

To investigate the role of poroelastic material on rupture propagation, we considered varying values of the Biot coefficient α. Additionally, we also consider the Gassmann equivalent elastic material. Because the Gassmann equivalent material neglects all fluid effects, we use a modified normal stress $\tilde{\sigma} = \sigma_{yy} - p_0$ to nucleate the rupture.

For the numerical simulation of the behaviour at the branch, we embed the fault in the cuboid $[-26000\,\text{m}, 22000\,\text{m}] \times [-10000\,\text{m}, 13100\,\text{m}] \times [-25000\,\text{m}, 0\,\text{m}]$. At $z = 0$ m, we impose

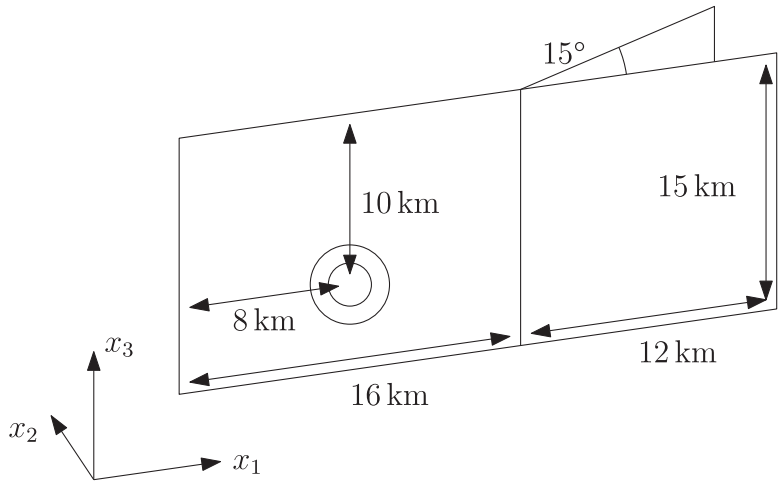

Figure 10. Sketch of the fault geometry for the fault branching experiment. The two circles on the main fault represent the nucleation area. The top of the fault aligns with the free surface.

Table 5. Generic material parameters for the dynamic rupture fault branching experiment.

Parameter	Description	Value	
E	Young's modulus	20.0×10^9	Pa
ν_P	Poisson ratio	0.25	
ρ_S	Solid density	2.50×10^3	$kg\,m^{-3}$
ρ_F	Fluid density	1.00×10^3	$kg\,m^{-3}$
ν	Fluid viscosity	0.001	Pas
κ	Permeability	1.00×10^{-14}	m^2
β	Fluid compressiblity	2.00×10^{-9}	Pa^{-1}
ϕ	Porosity	0.1	
α	Biot coefficient	0.3	up to 0.9

a free surface boundary condition, all other boundaries are absorbing. This domain is designed ensuring such that each point on the fault system is at least 10 km away from an absorbing boundary. We chose a mesh resolution of 100 m, which has proven to be sufficiently accurate in a previous convergence test (Wolf 2024). The scenario does not contain any material interfaces, so we do not expect pressure discontinuities (off the faults) as in section Section 3.1.2 The final mesh contains 2300 000 elements. As before, we use polynomials up to degree 5 as basis function. We used 30 nodes of Frontera, installed at the Texas Advanced Computing Center (TACC), to compute the numerical solution up to a time of 20 s.

Fig. 11 shows a comparison of the on-fault rupture dynamics and the seismic wave field after 11 s simulation time using the highest and lowest considered values of α, respectively. On the fault, the colour depicts the friction coefficient. In the purple areas, the friction coefficient is still at its initial (static) value, that is, the fault has not broken there. In the yellow areas, the friction coefficient has reduced to 0.3, the dynamic friction coefficient, that is, the fault has entirely weakened. The figure reveals that rupture jumps onto the branching fault in poroelastic material with $\alpha = 0.9$. In contrast, for the elastic equivalent material, only the main fault breaks and the branch is not activated. For $\alpha = 0.3$, poroelastic material and equivalent elastic material yield the same results, that is, the rupture does not propagate to the branch.

The Biot coefficient defines the partitioning of the total stress between the solid matrix and the pore fluid (e.g. De Simone *et al.* 2023). $\alpha = 0$ implies that the external stress results in no increase in pore pressure, and $\alpha = 1$ means that the external stress is equally partitioned between the stress applied to the solid matrix and pore pressure. To better understand the influence of the Biot coefficient, we perform a series of simulations for α ranging between 0.3 and 0.9 in steps of 0.05. This range covers the typically values of α (Detournay & Cheng 1993). We find that for $\alpha < 0.75$, the poroelastic and the Gassmann equivalent materials yield consistent results. However, for $\alpha \geq 0.75$, the results deviate. In the poroelastic case, both faults, the main fault and the branch, break, but in the elastic equivalent material only the main fault breaks.

In the elastic equivalent material, the branch never breaks in our simulations, whereas in the poroelastic material it breaks, if the Biot coefficient is sufficiently high. This implies that for high values of α, the elastic equivalent material is not a sufficient approximation of the full poroelastic behaviour. In the case of a low Biot coefficient, though, we do not see a qualitative difference between the poroelastic material and its elastic equivalent. At the same time, it is important to note that the response of poroelastic material does not depend on the Biot coefficient only, and, therefore, $\alpha = 0.75$ is not a universal threshold for applicability of the elastic equivalent material for rupture dynamics.

Additionally, this effect is recognizable in the release of seismic energy. We plot the on-fault measured seismic moment rate for all four scenarios in Fig. 12. For $\alpha = 0.3$, the moment release rate is almost identical, when comparing the poroelastic and elastic materials. For $\alpha = 0.9$, the picture is very different. The moment release rate for the elastic version remains consistent with that for $\alpha = 0.3$ (it is, in fact, slightly lower). However, in the poroelastic version, we observe an additional increase in seismic moment rate after around 5 s, corresponding to the simulation time when the rupture jumps onto the branch.

Finally, we briefly mention our analysis using poroelastic properties corresponding to real-world materials in (Detournay & Cheng 1993; Li & Zhang 2023) instead of generic material parameters (see Table 6). As expected, for all elastic equivalent material, only the main fault breaks and the branch remains intact. For charcoal granite (with very low α of 0.222), the elastic equivalent and poroelastic materials yield consistent results. However, for all other materials, we observe that for poroelastic rheology, the rupture diverted to the branch only, that is, the main fault remains intact behind the branching point. We thus observe qualitatively different behaviour than for

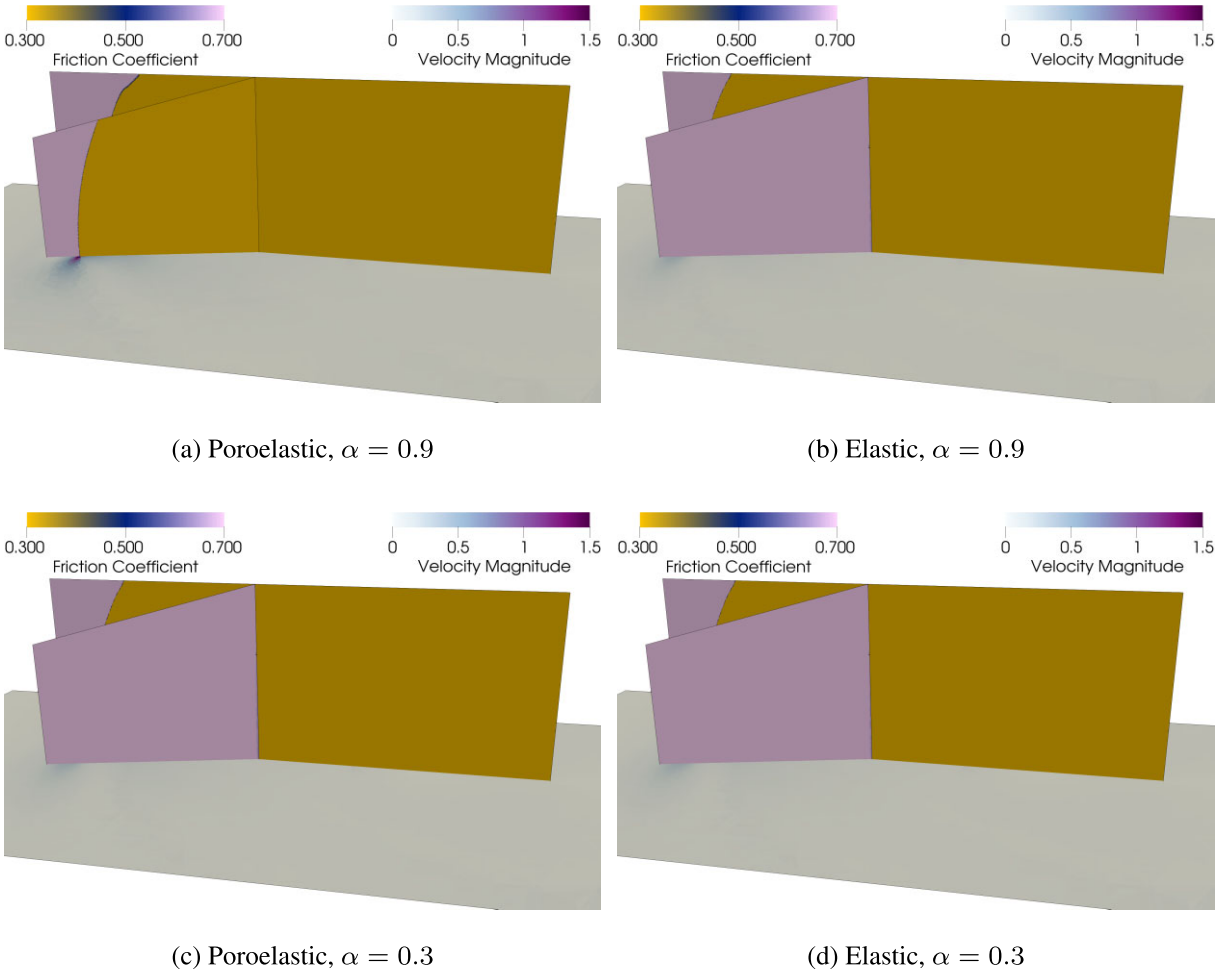

(a) Poroelastic, $\alpha = 0.9$ (b) Elastic, $\alpha = 0.9$

(c) Poroelastic, $\alpha = 0.3$ (d) Elastic, $\alpha = 0.3$

Figure 11. Friction coefficient and wave field in the fault branching scenario after 11 s. Yellow (darker) parts of the fault are entirely broken, purple (lighter) parts are yet intact. The top row shows the results for $\alpha = 0.9$ and the bottom row shows results for $\alpha = 0.3$. On the left, the simulation using the poroelastic material is shown. In the right column, the elastic equivalent is shown. Parts of the branched fault are cropped to visualize the main fault behind it. In addition, all snapshots in steps of 1 s for the $\alpha = 0.9$ case can be found in Figs C1 and C2 in the Appendix. Animations of this scenario can be found in the electronic supplement.

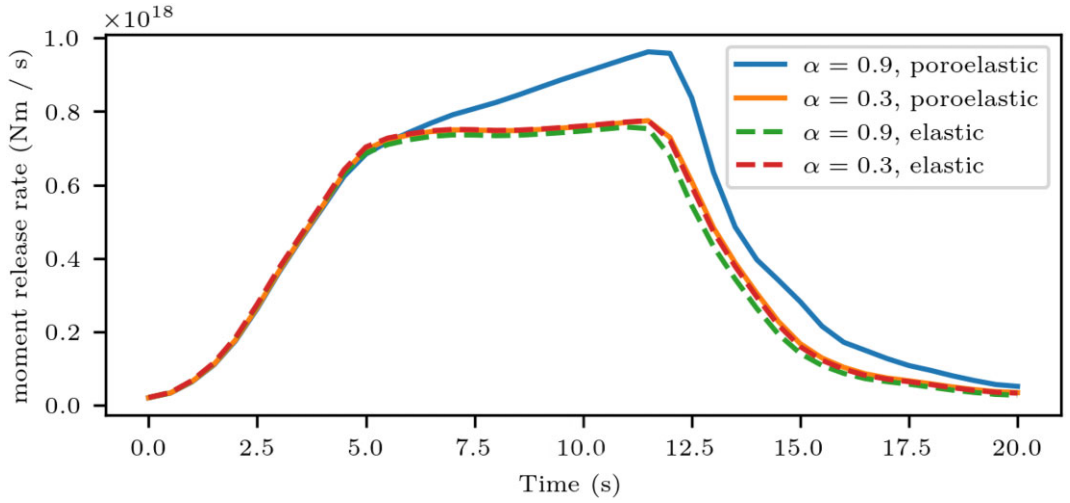

Figure 12. Seismic moment rate release over time for the four possible scenarios ($\alpha = 0.3/\alpha = 0.9$, poroelastic/elastic equivalent) of the branching scenario. For $\alpha = 0.3$, the lines are virtually identical. For $\alpha = 0.9$, we clearly see the additional release of seismic energy caused by the breaking branch after $t = 5$ s.

Table 6. Realistic material parameters for the poroelastic fault branching dynamic rupture experiment

Parameter	Charcoal granite	Pecos sandstone	Ruhr sandstone	Westerly granite	
K_S	45.0×10^9	39.0×10^9	36.0×10^9	45.0×10^9	Pa
ρ_S	3000	2590	2230	3000	$\mathrm{kg\,m^{-3}}$
λ_M	22.3×10^9	2.77×10^9	4.33×10^9	15.0×10^9	Pa
μ_M	19.0×10^9	5.90×10^9	13.0×10^9	15.0×10^9	Pa
κ	9.87×10^{-20}	7.90×10^{-16}	1.97×10^{-16}	3.95×10^{-19}	$\mathrm{m^2}$
T	2.0	2.0	2.0	2.0	
ϕ	0.02	0.2	0.02	0.01	
ρ_F	1000	1000	1000	1000	$\mathrm{kg\,m^{-3}}$
K_F	2.43×10^9	2.30×10^9	2.34×10^9	2.56×10^9	Pa
ν	0.001	0.001	0.001	0.001	Pa s
α	0.222	0.828	0.639	0.444	

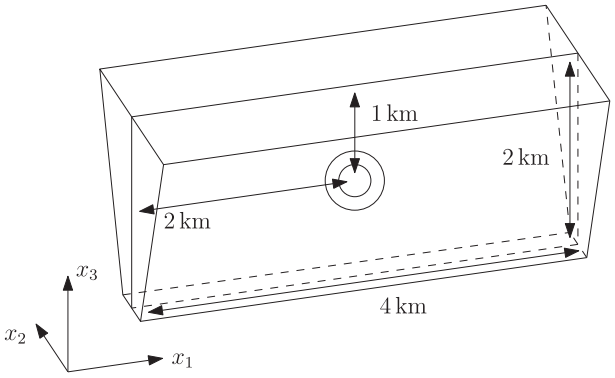

Figure 13. Sketch of the fault geometry together with the surrounding fault zone for the poroelastic fault zone dynamic rupture experiment. The two circles on the fault represent the nucleation area. The top of the fault aligns with the free surface boundary. At the top, the fault zone is 1000 m wide and at the bottom its width is reduced to 200 m.

the generic material properties above. This indicates that complex interaction between propagating dynamic rupture and dynamically induced pore-pressure variations determines vastly different dynamic triggering possibilities in a multifault system.

3.2.2 *Fault embedded in a poroelastic damage zone*

In the second example application, we analyse dynamic rupture across a fault embedded in a poroelastic fault damage zone. Natural damage zones contain highly fractured rocks (e.g. Chester *et al.* 1993; Ben-Zion & Sammis 2003) and can impact on rupture dynamic, for example, inducing pulse-like rupture (Huang & Ampuero 2011; Pelties *et al.* 2015). In distinction to previous studies, we here approximate a fault zone as a poroelastic material with higher permeability compared to the bedrock. Fig. 13 depicts the considered fault zone geometry with the strike-slip fault in the middle and the surrounding damaged zone. We consider the *fault zone* and *basement* materials from (Chang & Segall 2016), which can be found in Table 7. In the fault zone, the *S*-wave speed is reduced to approximately half of the value of the undamaged material in the basement. We also note that the Biot coefficients increases from 0.2 in the basement to 0.9 in the damaged zone.

We consider the same background stress σ as in the fault branching example (c.f. eq. 6) and the initial pressure

$$p_0 = \exp\left(-5 \times 10^{-6}\left((x)^2 + (y)^2 + (z + 1000)^2\right)\right) \cdot 8.0\,\mathrm{MPa}. \quad (8)$$

The fault is governed by linear slip weakening friction with $\mu_s = 0.7$, $\mu_d = 0.3$, $D_c = 0.1$ m. In this case, we do not consider shallow

Table 7. Material parameters for the poroelastic fault zone dynamic rupture scenario.

Parameter	Basement	Fault zone	
K_S	41.7×10^9	80.0×10^9	Pa
ρ_S	2.74×10^3	2.50×10^3	$\mathrm{kg\,m^{-3}}$
λ_M	16.7×10^9	4.00×10^9	Pa
μ_M	25.0×10^9	6.00×10^9	Pa
ϕ	0.05	0.02	
κ	2.00×10^{-17}	1.00×10^{-13}	$\mathrm{m^2}$
T	2.0	2.0	
K_F	2.50×10^9	2.50×10^9	Pa
ρ_F	1.00×10^3	1.00×10^3	$\mathrm{kg\,m^{-3}}$
ν	1.00×10^{-3}	1.00×10^{-3}	Pas
α	0.2	0.9	

frictional on-fault cohesion. The domain of interest is the cuboid $[-12\,\mathrm{km}, 12\,\mathrm{km}] \times [-10\,\mathrm{km}, 10\,\mathrm{km}] \times [-12\,\mathrm{km}, 0\,\mathrm{km}]$. We explicitly mesh the fault and the boundaries of the fault zone. The characteristic edge length is set to 25 m within the fault zone. with mesh coarsening towards the boundary outside the fault zone. The 3-D mesh consists of 2420 000 tetrahedrons.

We run the simulation for 5 s. We compare the results for the poroelastic material with those for the Gassmann equivalent material, just as we did in the fault branching experiment earlier. We do not expect to see as huge differences in the intensity of the rupture as can be found in (Li & Zhang 2023), who use a different mechanism to determine the pore pressure at the fault (c.f. Section 3.2). Fig. 14 compares the slip rate snapshots at the time 1.3 s. We observe almost identical rupture dynamics near the rupture fronts. However, further behind the rupture fronts, the solutions look very different. The rupture propagates in a pulse-like regime (e.g. Heaton 1990; Gabriel *et al.* 2012) in the poroelastic material, whereas in a crack-like mode in the elastic equivalent material. We conjecture that healing in the poroelastic material occurs as a consequence of reduced pore pressure at the fault due to reflected waves from the interface of the poroelastic damage zone.

4 DISCUSSION

Our models illustrate how the poroelastic material model affects seismic wave propagation and rupture dynamics in 3-D earthquake scenarios. In high-resolution seismic wave propagation simulations, we find an apparent pressure discontinuity across material interfaces, which increases the requirements on the numerical resolution. While it is known that poroelastic models require increased accuracy at material interfaces, (e.g. Zhang *et al.* 2022), the apparent pressure discontinuity has not yet been discussed. Nonetheless,

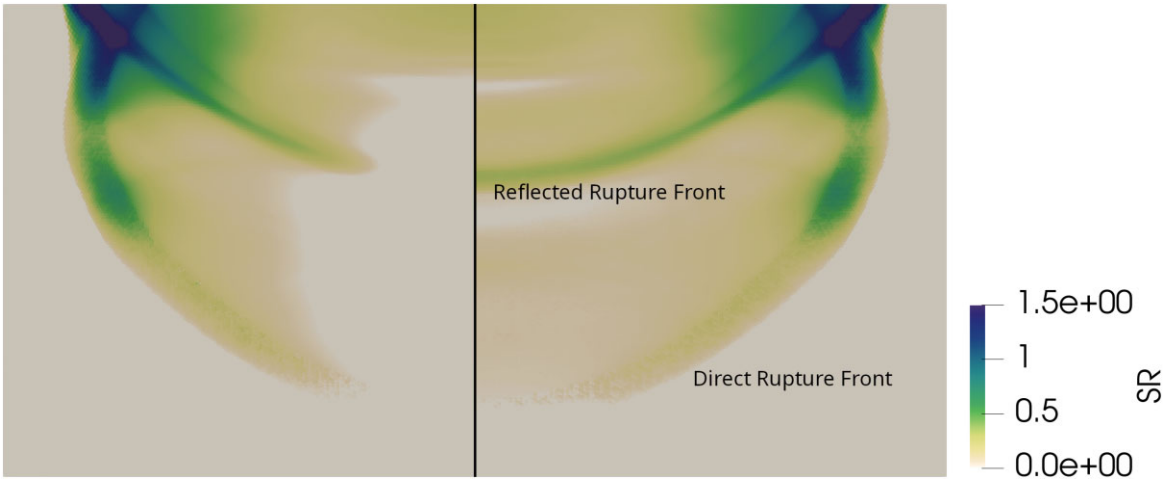

Figure 14. Slip rate magnitude $\|\vec{s}\|$ on the fault at time $t = 1.3$ s in the fault zone example. *Left*: the results for the poroelastic material. *Right*: the results for the elastic equivalent material. The upper rupture front is the one reflected from the free surface, the lower one propagates directly from the hypocentre. We clearly observe that the rupture arrests earlier in the poroelastic case, compared to the elastic equivalent.

we find this pronounced discontinuity in two independent numerical solutions—using SeisSol, a 3-D discontinuous Galerkin implementation, and using a 2-D finite-difference code. Therefore, we consider this effect to be a key component of the solution of the poroelastic wave equation.

In the case of the Sleipner reservoir scenario, we observe that the Gassmann equivalent serves as a suitable approximation to the poroelastic material describing the displacements of the matrix. However, the fluid pressure is not part of this equivalent elastic model, as it only considers the combined stress, that is, the stress sustained jointly by the matrix and the fluid. Consequently, how much of the total stress is sustained by the matrix and how much is sustained by the fluid is not captured by the Gassmann approximation.

In our dynamic rupture simulations, we observe that the pressure weakening effect, resulting from changes in effective fault strength due to fluid pressure variations, is not negligible. This effect substantially changes the dynamic rupture characteristics, including rupture velocity and fault-to-fault interaction. Therefore, we argue that the Gassmann equivalent should not be used when fluid pressure is expected to play a vital role in the specific application, as it does not adequately capture such dynamic effects.

The analysis of two complex 3-D dynamic rupture scenarios highlights that the pore pressure weakening changes the rupture characteristics significantly. In the first scenario, a secondary fault branch is dynamically activated additionally to the main fault due to poroelastic effects and releases more seismic energy. In the second scenario, dynamic rupture arrests more readily in the poroelastic case, illustrating the influence of fluid pressure on earthquake size.

Further studies are required to investigate the influence of additional material parameters beyond the Biot coefficient α, which may further influence rupture dynamics (Vyas *et al.* 2023) and seismic wave propagation. Also, analysis of poroelastic effects in more realistic models going beyond idealized benchmark scenarios is beyond the scope of this study.

Our model is limited to the low-frequency regime. We only consider frequencies up to the frequency above which flow through the pores would become turbulent. At frequencies of interest for most seismic applications, the flow in pores can be considered laminar, and thus the low-frequency regime suffices. An example of cases when this assumption is no longer valid are earthquake ground motions simulations in loose water saturated sediments (e.g. Gregor *et al.* 2021).

This study focuses on rupture dynamics governed by linear slip-weakening friction. Our findings indicate that the dynamic interactions between rupture and dynamically induced pore pressure variations are complex and highly nonlinear. Different effects may be expected for different friction laws and can be the focus of future work. For example, a combination with the more complex concept of rate-and-state friction can easily be integrated in our implementation of dynamic rupture in a poroelastic rheology.

5 CONCLUSIONS

We have successfully incorporated double-couple point sources in poroelastic media using the ADER-DG method within the earthquake simulation software SeisSol. We verified our implementation in canonical models using independent methods, confirming the accuracy and reliability of our approach. Furthermore, we demonstrated the potential of our method through a complex 3-D example of poroelastic seismic wave propagation at the Sleipner CCS site. Our analysis shows that the Gassmann elastic equivalent model yields almost identical results to the fully poroelastic model when focusing solely on solid particle velocities. However, the elastic equivalent fails to capture the evolution of pore pressure. Thus, results relying on the elastic equivalent model may be misleading in poroelastic dynamic rupture applications where fault(s) are exposed to dynamically induced variations of pore pressure.

By using suitable numerical fluxes, we have combined the dynamic rupture model with poroelastic rheology using the ADER-DG method. This enhancement to the SeisSol solver allowed us to investigate poroelastic effects on 3-D dynamic rupture in complex scenarios. While for seismic wave propagation problems we observe relatively limited effects of the poroelastic rheology that cannot be captured by the elastic equivalent model, we observe significant and intricate effects on dynamic rupture behaviour in the poroelastic models that cannot be captured in the elastic equivalent models. In a fault branching scenario, we observe that, depending on the Biot coefficient α, fault branching is facilitated or inhibited. In some cases, dynamic rupture diverted to the branch, leaving the

main fault unruptured. When the fault is surrounded by a poroelastic fault zone, we observe pulse-like rupture with a healing front induced by reduced pore pressure due to reflected waves from the boundaries of the poroelastic damage zone.

This study is, to the best of our knowledge, the first where a 3-D tetrahedral mesh is used to analyse dynamic rupture propagating on a fault system with complicated geometry embedded in poroelastic media. This advancement allows considering more complicated fault geometries, such as fault branching, intersections and poroelastic fault zones. The observed differences between results for the poroelastic model and the Gassmann equivalent model suggest that poroelastic effects may play a crucial role in explaining complex and unexpected dynamics rupture patterns. Since the algorithms have been implemented in the open-source solver SeisSol, this study can be a starting point for other researchers to include poroelastic effects in their models.

ACKNOWLEDGMENTS

We thank Eric M. Dunham and Dmitry Garagash for helpful discussions on dynamic rupture in poroelastic media. We furthermore thank the Editor Sidao Ni and Assistant Editor Louise Alexander as well as two anonymous reviewers for their constructive feedback, which helped improving the manuscript. We thank the Leibniz Supercomputing Centre of the Bavarian Academy of Sciences and Humanities for granting compute time in the project pr83no and pn49ha and the Texas Advanced Computing Center for granting compute time in the project EAR22007. SW and MB acknowledge funding by the Competence Network for Scientific High Performance Computing in Bavaria (KONWIHR). SW, A-AG and MB acknowledge funding from the European High Performance Computing Joint Undertaking (JU) under grant agreement no. 101093038 and from the German Federal Ministry of Education and Research (BMBF), both for the ChEESE-2P cluster of excellence. A-AG acknowledges additional support by the European Union's Horizon 2020 Research and Innovation Programme (TEAR, grant number 852992), Horizon Europe (DT-GEO, grant number 101058129, and Geo-INQUIRE, grant number 101058518), the National Aeronautics and Space Administration (80NSSC20K0495), the National Science Foundation (grant numbers EAR-2225286, EAR-2121568, OAC-2139536, OAC-2311208) and the Southern California Earthquake Center (SCEC awards 22135, 23121).

SUPPORTING INFORMATION

Supplementary data are available at *GJIRAS* online.
Please note: Oxford University Press is not responsible for the content or functionality of any supporting materials supplied by the authors. Any queries (other than missing material) should be directed to the corresponding author for the paper.

DATA AVAILABILITY

The simulation results can be reproduced with SeisSol version v1.1.3 (https://doi.org/10.5281/zenodo.10594058) using the input data available from zenodo (https://zenodo.org/records/11401733).

REFERENCES

Aagaard, B.T., Knepley, M.G. & Williams, C.A., 2013. A domain decomposition approach to implementing fault slip in finite-element models of quasi-static and dynamic crustal deformation, *J. Geophys. Res. Solid Earth,* **118**(6), 3059–3079.

Aki, K. & Richards, P., 2002. *Quantitative Seismology, 2nd edn,* University Science Books, U.S., Sausalito, California.

Andrews, D.J., 1976. Rupture velocity of plane strain shear cracks, *J. geophys. Res.,* **81**(32), 5679–5687.

Barall, M., 2009. A grid-doubling finite-element technique for calculating dynamic three-dimensional spontaneous rupture on an earthquake fault, *Geophys. J. Int.,* **178**(2), 845–859.

Ben-Zion, Y. & Sammis, C.G., 2003. Characterization of Fault Zones, *Pure appl. Geophys.,* **160**(3), 677–715.

Berryman, J.G., 1980. Confirmation of Biot's theory, *Appl. Phys. Lett.,* **37**(4), 382–384.

Biot, M.A., 1956a. Theory of propagation of elastic waves in a fluid-saturated porous solid. I. Low-frequency range, *J. acoust. Soc. Am.,* **28**(2), 168–178.

Biot, M.A., 1956b. Theory of propagation of elastic waves in a fluid-saturated porous solid. II. Higher frequency range, *J. acoust. Soc. Am.,* **28**(2), 179–191.

Biot, M.A., 1956c. Theory of deformation of a porous viscoelastic anisotropic solid, *J. Appl. Phys.,* **27**(5), 459–467.

Biot, M.A., 1962. Mechanics of deformation and acoustic propagation in porous media, *J. Appl. Phys.,* **33**(4), 1482–1498.

Carcione, J.M., 2001. Energy balance and fundamental relations in dynamic anisotropic poro-viscoelasticity, *Proc. R. Soc. Lond. Ser. A: Math. Phys. Eng. Sci.,* **457,** 331–348.

Carcione, J.M., 2015. *Wave Fields in Real Media, 3rd edn,* Elsevier, Oxford.

Carcione, J.M., Morency, C. & Santos, J.E., 2010. Computational poroelasticity—a review, *Geophysics,* **75,** 75A229–75A243.

Castagna, J.P. & Backus, M.M., 1993. *Offset-Dependent Reflectivity—Theory and Practice of AVO Analysis,* Society of Exploration Geophysicists.

Chang, K.W. & Segall, P., 2016. Injection-induced seismicity on basement faults including poroelastic stressing, *J. Geophys. Res. Solid Earth,* **121**(4), 2708–2726.

Chester, F.M., Evans, J.P. & Biegel, R.L., 1993. Internal structure and weakening mechanisms of the san andreas fault, *J. Geophys. Res. Solid Earth,* **98**(B1), 771–786.

Cruz-Atienza, V.M. & Virieux, J., 2004. Dynamic rupture simulation of non-planar faults with a finite-difference approach, *Geophys. J. Int.,* **158**(3), 939–954.

Day, S.M., 1982. Three-dimensional finite difference simulation of fault dynamics: rectangular faults with fixed rupture velocity, *Bull. seism. Soc. Am.,* **72**(3), 705–727.

Day, S.M., Dalguer, L.A., Lapusta, N. & Liu, Y., 2005. Comparison of finite difference and boundary integral solutions to three-dimensional spontaneous rupture, *J. geophys. Res.,* **110**(B12), 1–23.

De Barros, L., Dietrich, M. & Valette, B., 2010. Full waveform inversion of seismic waves reflected in a stratified porous medium: full waveform inversion in porous medium, *Geophys. J. Int.,* **182**(3), 1543–1556.

de la Puente, J., 2008. Seismic wave simulation for complex rheologies on unstructured meshes, *Ph.D. thesis*, Ludwig—Maximilians—Universität München, Munich.

de la Puente, J., Dumbser, M., Käser, M. & Igel, H., 2008. Discontinuous Galerkin methods for wave propagation in poroelastic media, *Geophysics,* **73**(5), T77–T97.

de la Puente, J., Ampuero, J.-P. & Käser, M., 2009. Dynamic rupture modelling on unstructured meshes using a discontinuous Galerkin method, *J. Geophys. Res. Solid Earth,* **114**(B10), doi:10.1029/2008JB006271.

De Simone, S., Darcel, C., Kasani, H.A., Mas Ivars, D. & Davy, P., 2023. Equivalent Biot and Skempton poroelastic coefficients for a fractured rock mass from a DFN approach, *Rock Mech. Rock Eng.,* **56**(12), 8907–8925.

Detournay, E. & Cheng, A.H.D., 1993. Fundamentals of poroelasticity, in *Analysis and Design Methods,* pp. 113–171, ed., Fairhurst, C., Pergamon, Oxford.

Duan, B., 2012. Dynamic rupture of the 2011 M_w 9.0 Tohoku-Oki earthquake: roles of a possible subducting seamount, *J. Geophys. Res. Solid Earth,* **117**(B5), 1–16.

Dumbser, M. & Käser, M., 2006. An arbitrary high-order discontinuous Galerkin method for elastic waves on unstructured meshes - II. The three-dimensional isotropic case, *Geophys. J. Int.,* **167**(1), 319–336.

Dumbser, M., Balsara, D.S., Toro, E.F. & Munz, C.-D., 2008. A unified framework for the construction of one-step finite volume and discontinuous Galerkin schemes on unstructured meshes, *J. Comput. Phys.,* **227**(18), 8209–8253.

Dunham, E.M. & Rice, J.R., 2008. Earthquake slip between dissimilar poroelastic materials, *J. Geophys. Res. Solid Earth,* **113**(B9), doi:10.1029/2007JB005405.

Dupuy, B., Garambois, S. & Virieux, J., 2016. Estimation of rock physics properties from seismic attributes—Part 1: Strategy and sensitivity analysis, *Geophysics,* **81**(3), M35–M53.

Duru, K. & Dunham, E.M., 2016. Dynamic earthquake rupture simulations on nonplanar faults embedded in 3-D geometrically complex, heterogeneous elastic solids, *J. Comput. Phys.,* **305,** 185–207.

Duru, K., Rannabauer, L., Gabriel, A.-A. & Igel, H., 2021. A new discontinuous Galerkin method for elastic waves with physically motivated numerical fluxes, *J. Sci. Comput.,* **88**(3), 1–32.

Dutta, N.C. & Odé, H., 1983. Seismic reflections from a gas-water contact, *Geophysics,* **48**(2), 148–162.

Ely, G.P., Day, S.M. & Minster, J.-B., 2009. A support-operator method for 3-D rupture dynamics, *Geophys. J. Int.,* **177**(3), 1140–1150.

Ely, G.P., Day, S.M. & Minster, J.-B., 2010. Dynamic rupture models for the Southern San Andreas fault, *Bull. seism. Soc. Am.,* **100**(1), 131–150.

Equinor 2019. Sleipner 2019 benchmark model, https://co2datashare.org/dataset/sleipner-2019-benchmark-model.

Gabriel, A.-A., 2021. A unified first-order hyperbolic model for nonlinear dynamic rupture processes in diffuse fracture zones, *Philos. Trans. R. Soc. A,* **379**(2196), 20 200 130, doi:10.1098/rsta.2020.0130.

Gabriel, A.-A., Ampuero, J.-P., Dalguer, L.A. & Mai, P.M., 2012. The transition of dynamic rupture styles in elastic media under velocity-weakening friction, *J. Geophys. Res. Solid Earth,* **117**(B9), 01480227. doi:10.1029/2012JB009468.

Gabriel, A.-A., Ulrich, T., Marchandon, M., Biemiller, J. & Rekoske, J., 2023. 3-D dynamic rupture modelling of the 6 February 2023, Kahramanmaraş, Turkey M_w 7.8 and 7.7 earthquake doublet using early observations, *The Seismic Record,* **3**(4), 342–356.

Galis, M., Ampuero, J.P., Mai, P.M. & Cappa, F., 2017. Induced seismicity provides insight into why earthquake ruptures stop, *Sci. Adv.,* **3**(12), eaap7528, doi:10.1126/sciadv.aap7528.

Gardner, G. H.F., Gardner, L.W. & Gregory, A.R., 1974. Formation velocity and density; the diagnostic basics for stratigraphic traps, *Geophysics,* **39**(6), 770–780.

Gassmann, F., 1951. Über die Elastizität poröser Medien , in *Vierteljahrsschrift der naturforschenden Gesellschaft in Zürich,* Vol. **96,** pp. 1–21. ed. Pelissier, M. A., Soc. Expl. Geoph, Tulsa.

Gassner, G., Dumbser, M., Hindenlang, F. & Munz, C.-D., 2011. Explicit one-step time discretizations for discontinuous Galerkin and finite volume schemes based on local predictors, *J. Comput. Phys.,* **230**(11), 4232–4247.

Gregor, D., Moczo, P., Kristek, J., Mesgouez, A., Lefeuve-Mesgouez, G. & Kristekova, M., 2021. Subcell-resolution finite-difference modelling of seismic waves in Biot and JKD poroelastic media, *Geophys. J. Int.,* **224**(2), 760–794.

Gregor, D., Moczo, P., Kristek, J., Mesgouez, A., Lefeuve-Mesgouez, G., Morency, C., Diaz, J. & Kristekova, M., 2022. Seismic waves in medium with poroelastic/elastic interfaces: a two-dimensional P-SV finite-difference modelling, *Geophys. J. Int.,* **228**(1), 551–588.

Harris, R.A. *et al.*, 2009. The SCEC/USGS dynamic earthquake rupture code verification exercise, *Seism. Res. Lett.,* **80**(1), 119–126.

Harris, R.A. *et al.*, 2011. Verifying a computational method for predicting extreme ground motion, *Seism. Res. Lett.,* **82**(5), 638–644.

Harris, R.A. *et al.*, 2018. A suite of exercises for verifying dynamic earthquake rupture codes, *Seism. Res. Lett.,* **89**(3), 1146–1162.

Harris, R.A. *et al.*, 2021. A geology and geodesy based model of dynamic earthquake rupture on the Rodgers Creek-Hayward-Calaveras fault system, California, *J. Geophys. Res. Solid Earth,* **126**(3), e2020JB020577, doi:10.1029/2020JB020577.

Hayek, J.N., May, D.A., Pranger, C. & Gabriel, A.-A., 2023. A diffuse interface method for earthquake rupture dynamics based on a phase-field model, *J. Geophys. Res. Solid Earth,* **128**(12), e2023JB027143, doi:10.1029/2023JB027143.

Heaton, T.H., 1990. Evidence for and implications of self-healing pulses of slip in earthquake rupture, *Phys. Earth planet. Inter.,* **64,** doi:10.1016/0031-9201(90)90002-F.

Heimisson, E.R., Rudnicki, J. & Lapusta, N., 2021. Dilatancy and compaction of a rate-and-state fault in a poroelastic medium: linearized stability analysis, *J. Geophys. Res. Solid Earth,* **126**(8), e2021JB022071, doi:10.1029/2021JB022071.

Hesthaven, J.S. & Warburton, T., 2008. Nodal discontinuous Galerkin methods: algorithms, analysis, and applications, texts in applied mathematics, Springer-Verlag, New York.

Huang, Y. & Ampuero, J.-P., 2011. Pulse-like ruptures induced by low-velocity fault zones, *J. Geophys. Res. Solid Earth,* **116**(B12), _eprint: https://onlinelibrary.wiley.com/doi/pdf/10.1029/2011JB008684.

Jha, B. & Juanes, R., 2014. Coupled multiphase flow and poromechanics: a computational model of pore pressure effects on fault slip and earthquake triggering, *Water Resour. Res.,* **50**(5), 3776–3808.

Kammer, D.S. *et al.*, 2024. Earthquake energy dissipation in a fracture mechanics framework, *Nat. Commun.,* **15**(1), 4736, doi:10.1038/s41467-024-47970-6.

Kaneko, Y., Lapusta, N. & Ampuero, J.-P., 2008. Spectral element modelling of spontaneous earthquake rupture on rate and state faults: Effect of velocity-strengthening friction at shallow depths, *J. Geophys. Res. Solid Earth,* **113**(B9), 1–17.

Karpfinger, F., Müller, T.M. & Gurevich, B., 2009. Green's functions and radiation patterns in poroelastic solids revisited, *Geophys. J. Int.,* **178**(1), 327–337.

Kristekova, M., Kristek, J., Moczo, P. & Day, S.M., 2006. Misfit criteria for quantitative comparison of seismograms, *Bull. seism. Soc. Am.,* **96**(5), 1836–1850.

Kristekova, M., Kristek, J. & Moczo, P., 2009. Time-frequency misfit and goodness-of-fit criteria for quantitative comparison of time signals, *Geophys. J. Int.,* **178**(2), 813–825.

Käser, M., Hermann, V. & de la Puente, J., 2008. Quantitative accuracy analysis of the discontinuous Galerkin method for seismic wave propagation, *Geophys. J. Int.,* **173**(3), 990–999.

LeVeque, R.J., 2002. *Finite Volume Methods for Hyperbolic Problems, Cambridge Texts in Applied Mathematics,* Cambridge University Press, Cambridge.

Li, Z. & Zhang, H., 2023. Time-domain Green's function in poroelastic mediums and its application to 3-D spontaneous rupture simulation, *Geophys. J. Int.,* **234**(3), 2231–2254.

Masson, Y.J., Pride, S.R. & Nihei, K.T., 2006. Finite difference modelling of Biot's poroelastic equations at seismic frequencies, *J. geophys. Res.,* **111**(B10), 1–13.

Mavko, G., Mukerji, T. & Dvorkin, J., 2009. *The Rock Physics Handbook: Tools for Seismic Analysis of Porous Media 2nd edn,* Cambridge University Press, Cambridge.

Moczo, P., Jozef, K. & Martin, G., 2014. *The Finite-Difference Modelling of Earthquake Motions: Waves and Ruptures,* Cambridge University Press, Cambridge.

Moczo, P., Gregor, D., Kristek, J. & de la Puente, J., 2019. A discrete representation of material heterogeneity for the finite-difference modelling of seismic wave propagation in a poroelastic medium, *Geophys. J. Int.,* **216**(2), 1072–1099.

Morency, C., Luo, Y. & Tromp, J., 2011. Acoustic, elastic and poroelastic simulations of CO2 sequestration crosswell monitoring based on spectral-element and adjoint methods: CO2 sequestration monitoring, *Geophys. J. Int.,* **185**(2), 955–966.

Oglesby, D.D., Archuleta, R.J. & Nielsen, S.B., 1998. Earthquakes on dipping faults: the effects of broken symmetry, *Science,* **280**(5366), 1055–1059.

Okubo, K., Rougier, E., Lei, Z. & Bhat, H.S., 2020. Modeling earthquakes with off-fault damage using the combined finite-discrete element method, *Comput. Part. Mech.,* **7**(5), 1057–1072.

Pampillón, P., Santillán, D., Mosquera, J.C. & Cueto-Felgueroso, L., 2018. Dynamic and quasi-dynamic modelling of injection-induced earthquakes in poroelastic media, *J. Geophys. Res.: Solid Earth,* **123**(7), 5730–5759.

Pampillón, P., Santillán, D., Mosquera, J.C. & Cueto-Felgueroso, L., 2023. The role of pore fluids in supershear earthquake ruptures, *Sci. Rep.,* **13**(1), 1–10.

Pelties, C., de la Puente, J., Ampuero, J.-P., Brietzke, G.B. & Käser, M., 2012a. Three-dimensional dynamic rupture simulation with a high-order discontinuous Galerkin method on unstructured tetrahedral meshes, *J. Geophys. Res. Solid Earth,* **117**(B2), doi:10.1029/2011JB008857.

Pelties, C., de la Puente, J., Ampuero, J.-P., Brietzke, G.B. & Käser, M., 2012b. Three-dimensional dynamic rupture simulation with a high-order discontinuous Galerkin method on unstructured tetrahedral meshes, *J. Geophys. Res. Solid Earth,* **117**(B2), 1–15.

Pelties, C., Huang, Y. & Ampuero, J.-P., 2015. Pulse-like rupture induced by three-dimensional fault zone flower structures, *Pure appl. Geophys.,* **172**(5), 1229–1241.

Plona, T.J., 1980. Observation of a second bulk compressional wave in a porous medium at ultrasonic frequencies, *Appl. Phys. Lett.,* **36**(4), 259–261.

Ramos, M.D., Thakur, P., Huang, Y., Harris, R.A. & Ryan, K.J., 2022. Working with dynamic earthquake rupture models: a practical guide, *Seism. Res. Lett.,* **93**(4), 2096–2110.

Rudnicki, J.W. & Rice, J.R., 2006. Effective normal stress alteration due to pore pressure changes induced by dynamic slip propagation on a plane between dissimilar materials, *J. Geophys. Res. Solid Earth,* **111**(B10), doi:10.1029/2006JB004396.

Sambridge, M., 1999. Geophysical inversion with a neighbourhood algorithm—I. Searching a parameter space, *Geophys. J. Int.,* **138**(2), 479–494.

Shapiro, S.A., 2015. *Fluid-induced Seismicity,* Cambridge University Press, Cambridge.

Song, Y. & Rudnicki, J.W., 2017. Plane-strain shear dislocation on a leaky plane in a poroelastic solid, *J. Appl. Mech.,* **84**(2), 021 008, doi:10.1115/1.4035179.

Taufiqurrahman, T., Gabriel, A., Ulrich, T., Valentová, L. & Gallovič, F., 2022. Broad-band dynamic rupture modelling with fractal fault roughness, frictional heterogeneity, viscoelasticity and topography: the 2016 M_w 6.2 Amatrice, Italy earthquake, *Geophys. Res. Lett.,* **49**(22), e2022GL098872, doi:10.1029/2022GL098872.

Traub, B., 2008. 2ReMoVe–WP 3.4: Sleipner AVO study on synthetic Sleipner data, Tech. rep., SINTEF Petroleum Research.

Ulrich, T., Gabriel, A.-A., Ampuero, J.-P. & Xu, W., 2019. Dynamic viability of the 2016 M_w 7.8 Kaikōura earthquake cascade on weak crustal faults, *Nat. Commun.,* **10**(1), 1–16.

Uphoff, C., 2020. Flexible model extension and optimization for earthquake simulations at extreme scales, *Ph.D. thesis*, Technische Universität München.

Uphoff, C. & Bader, M., 2020. Yet another tensor toolbox for discontinuous Galerkin methods and other applications, *ACM Trans. Math. Softw.,* **46**(4), 34:1–34:40.

Uphoff, C., Rettenberger, S., Bader, M., Madden, E.H., Ulrich, T., Wollherr, S. & Gabriel, A.-A., 2017. Extreme scale multi-physics simulations of the Tsunamigenic 2004 Sumatra megathrust earthquake, in *Proceedings of the International Conference for High Performance Computing, Networking, Storage and Analysis, SC '17,* pp. 21:1–21:16, ACM, New York, NY, USA.

Vernik, L., Fisher, D. & Bahret, S., 2002. Estimation of net-to-gross from *P* and *S* impedance in deepwater turbidites, *Leading Edge,* **21**(4), 380–387.

Virieux, J. & Madariaga, R., 1982. Dynamic faulting studied by a finite difference method, *Bull. seism. Soc. Am.,* **72**(2), 345–369.

Vyas, J.C., Gabriel, A.-A., Ulrich, T., Mai, P.M. & Ampuero, J.-P., 2023. How does thermal pressurization of pore fluids affect 3D strike-slip earthquake dynamics and ground motions?, *Bull. seism. Soc. Am.,* **113**(5), 1992–2008.

Wolf, S., 2024. High-performance earthquake simulations with advanced material models, *Ph.D. thesis*, Technische Universität München.

Wolf, S., Galis, M., Uphoff, C., Gabriel, A.-A., Moczo, P., Gregor, D. & Bader, M., 2022. An efficient ADER-DG local time stepping scheme for 3D HPC simulation of seismic waves in poroelastic media, *J. Comput. Phys.,* **455,** 1–29.

Yan, H., 2017. Rock physics inversion for CO2 characterization at Sleipner, Master's thesis, NTNU.

Yang, Z. & Juanes, R., 2018. Two sides of a fault: grain-scale analysis of pore pressure control on fault slip, *Phys. Rev. E,* **97**(2), 022 906, doi:10.1103/PhysRevE.97.022906.

Zhang, H., Sun, Y.-C., Ren, H., Zhang, W., Huang, Q. & Chen, X., 2022. Discontinuous curvilinear collocated grid combined with nonuniform time step Runge-Kutta scheme for poroelastic finite-difference modelling, *Geophysics,* **88**(1), T1–T12.

Zhang, Z., Zhang, W. & Chen, X., 2014. Three-dimensional curved grid finite-difference modelling for non-planar rupture dynamics, *Geophys. J. Int.,* **199**(2), 860–879.

Zhu, X. & McMechan, G.A., 1991. Numerical simulation of seismic responses of poroelastic reservoirs using Biot theory, *Geophysics,* **56**(3), 328–339.

APPENDIX A: FLUX AND SOURCE MATRICES FOR THE POROELASTIC WAVE EQUATION

Here, we summarize the isotropic version of the matrices A, B, C and E from eq. (1) as they are given by de la Puente (2008). SeisSol and the ADER-DG discretization expect the governing equations to be expressed in such a first-order formulation. The basic material parameters are the solid density ρ_S and the bulk modulus K_S. Furthermore, the Lamé parameters λ_M, μ_M of the matrix together with porosity ϕ, permeability κ and tortuosity T. The fluid is described by the bulk modulus K_F, the density ρ_F and the viscosity ν. Biot coefficient is defined as $1 - \frac{K_M}{K_S}$ and the coupling modulus is defined as

$$M = \frac{K_S}{1 - \phi - K_M/K_S + \phi K_S/K_F}, \tag{A1}$$

where the matrix bulk modulus is given by $K_M = \lambda_M + \frac{2}{3}\mu_M$. The flux and source matrices now read:

$$A = \left(\begin{array}{cccccc|cccccc}
0 & 0 & 0 & 0 & 0 & 0 & \lambda_M + 2\mu_M + M\alpha^2 & 0 & 0 & 0 & M\alpha & 0 & 0 \\
0 & 0 & 0 & 0 & 0 & 0 & \lambda_M + M\alpha^2 & 0 & 0 & 0 & M\alpha & 0 & 0 \\
0 & 0 & 0 & 0 & 0 & 0 & \lambda_M + M\alpha^2 & 0 & 0 & 0 & M\alpha & 0 & 0 \\
0 & 0 & 0 & 0 & 0 & 0 & 0 & \mu_M & 0 & 0 & 0 & 0 & 0 \\
0 & 0 & 0 & 0 & 0 & 0 & 0 & 0 & 0 & 0 & 0 & 0 & 0 \\
0 & 0 & 0 & 0 & 0 & 0 & 0 & 0 & \mu_M & 0 & 0 & 0 & 0 \\
\hline
\frac{1}{\rho_1} & 0 & 0 & 0 & 0 & 0 & 0 & 0 & 0 & \frac{\beta_1}{\rho_1} & 0 & 0 & 0 \\
0 & 0 & 0 & \frac{1}{\rho_1} & 0 & 0 & 0 & 0 & 0 & 0 & 0 & 0 & 0 \\
0 & 0 & 0 & 0 & 0 & \frac{1}{\rho_1} & 0 & 0 & 0 & 0 & 0 & 0 & 0 \\
0 & 0 & 0 & 0 & 0 & 0 & -M\alpha & 0 & 0 & 0 & -M & 0 & 0 \\
\frac{1}{\rho_2} & 0 & 0 & 0 & 0 & 0 & 0 & 0 & 0 & \frac{\beta_2}{\rho_2} & 0 & 0 & 0 \\
0 & 0 & 0 & \frac{1}{\rho_2} & 0 & 0 & 0 & 0 & 0 & 0 & 0 & 0 & 0 \\
0 & 0 & 0 & 0 & 0 & \frac{1}{\rho_2} & 0 & 0 & 0 & 0 & 0 & 0 & 0
\end{array}\right), \tag{A2}$$

$$B = \left(\begin{array}{ccccccc|ccccccc}
0 & 0 & 0 & 0 & 0 & 0 & 0 & \lambda_M + M\alpha^2 & 0 & 0 & 0 & M\alpha & 0 \\
0 & 0 & 0 & 0 & 0 & 0 & 0 & \lambda_M + 2\mu_M + M\alpha^2 & 0 & 0 & 0 & M\alpha & 0 \\
0 & 0 & 0 & 0 & 0 & 0 & 0 & \lambda_M + M\alpha^2 & 0 & 0 & 0 & M\alpha & 0 \\
0 & 0 & 0 & 0 & 0 & 0 & \mu_M & 0 & 0 & 0 & 0 & 0 & 0 \\
0 & 0 & 0 & 0 & 0 & 0 & 0 & 0 & \mu_M & 0 & 0 & 0 & 0 \\
0 & 0 & 0 & 0 & 0 & 0 & 0 & 0 & 0 & 0 & 0 & 0 & 0 \\
\hline
0 & 0 & 0 & \frac{1}{\rho_1} & 0 & 0 & 0 & 0 & 0 & 0 & 0 & 0 & 0 \\
0 & \frac{1}{\rho_1} & 0 & 0 & 0 & 0 & 0 & 0 & 0 & \frac{\beta_1}{\rho_1} & 0 & 0 & 0 \\
0 & 0 & 0 & 0 & \frac{1}{\rho_1} & 0 & 0 & 0 & 0 & 0 & 0 & 0 & 0 \\
0 & 0 & 0 & 0 & 0 & 0 & 0 & -M\alpha & 0 & 0 & 0 & -M & 0 \\
0 & 0 & 0 & \frac{1}{\rho_2} & 0 & 0 & 0 & 0 & 0 & 0 & 0 & 0 & 0 \\
0 & \frac{1}{\rho_2} & 0 & 0 & 0 & 0 & 0 & 0 & 0 & \frac{\beta_2}{\rho_2} & 0 & 0 & 0 \\
0 & 0 & 0 & 0 & \frac{1}{\rho_2} & 0 & 0 & 0 & 0 & 0 & 0 & 0 & 0
\end{array}\right), \tag{A3}$$

$$C = \left(\begin{array}{ccccccccc|ccccc}
0 & 0 & 0 & 0 & 0 & 0 & 0 & 0 & \lambda_M + M\alpha^2 & 0 & 0 & 0 & M\alpha \\
0 & 0 & 0 & 0 & 0 & 0 & 0 & 0 & \lambda_M + M\alpha^2 & 0 & 0 & 0 & M\alpha \\
0 & 0 & 0 & 0 & 0 & 0 & 0 & 0 & \lambda_M + 2\mu_M + M\alpha^2 & 0 & 0 & 0 & M\alpha \\
0 & 0 & 0 & 0 & 0 & 0 & 0 & 0 & 0 & 0 & 0 & 0 & 0 \\
0 & 0 & 0 & 0 & 0 & 0 & 0 & \mu_M & 0 & 0 & 0 & 0 & 0 \\
0 & 0 & 0 & 0 & 0 & 0 & \mu_M & 0 & 0 & 0 & 0 & 0 & 0 \\
\hline
0 & 0 & 0 & 0 & 0 & \frac{1}{\rho_1} & 0 & 0 & 0 & 0 & 0 & 0 & 0 \\
0 & 0 & 0 & 0 & \frac{1}{\rho_1} & 0 & 0 & 0 & 0 & 0 & 0 & 0 & 0 \\
0 & 0 & \frac{1}{\rho_1} & 0 & 0 & 0 & 0 & 0 & 0 & \frac{\beta_1}{\rho_1} & 0 & 0 & 0 \\
0 & 0 & 0 & 0 & 0 & 0 & 0 & 0 & -M\alpha & 0 & 0 & 0 & -M \\
0 & 0 & 0 & 0 & 0 & \frac{1}{\rho_2} & 0 & 0 & 0 & 0 & 0 & 0 & 0 \\
0 & 0 & 0 & 0 & \frac{1}{\rho_2} & 0 & 0 & 0 & 0 & 0 & 0 & 0 & 0 \\
0 & 0 & \frac{1}{\rho_2} & 0 & 0 & 0 & 0 & 0 & 0 & \frac{\beta_2}{\rho_2} & 0 & 0 & 0
\end{array}\right), \tag{A4}$$

and

$$E = \left(\begin{array}{cccccccccccc|ccc}
0 & 0 & 0 & 0 & 0 & 0 & 0 & 0 & 0 & 0 & 0 & 0 & 0 & 0 \\
0 & 0 & 0 & 0 & 0 & 0 & 0 & 0 & 0 & 0 & 0 & 0 & 0 & 0 \\
0 & 0 & 0 & 0 & 0 & 0 & 0 & 0 & 0 & 0 & 0 & 0 & 0 & 0 \\
0 & 0 & 0 & 0 & 0 & 0 & 0 & 0 & 0 & 0 & 0 & 0 & 0 & 0 \\
0 & 0 & 0 & 0 & 0 & 0 & 0 & 0 & 0 & 0 & 0 & 0 & 0 & 0 \\
0 & 0 & 0 & 0 & 0 & 0 & 0 & 0 & 0 & 0 & 0 & 0 & 0 & 0 \\
\hline
0 & 0 & 0 & 0 & 0 & 0 & 0 & 0 & 0 & 0 & \frac{\beta_1 v}{\rho_1 \kappa} & 0 & 0 \\
0 & 0 & 0 & 0 & 0 & 0 & 0 & 0 & 0 & 0 & 0 & \frac{\beta_1 v}{\rho_1 \kappa} & 0 \\
0 & 0 & 0 & 0 & 0 & 0 & 0 & 0 & 0 & 0 & 0 & 0 & \frac{\beta_1 v}{\rho_1 \kappa} \\
0 & 0 & 0 & 0 & 0 & 0 & 0 & 0 & 0 & 0 & 0 & 0 & 0 \\
0 & 0 & 0 & 0 & 0 & 0 & 0 & 0 & 0 & 0 & \frac{\beta_2 v}{\rho_2 \kappa} & 0 & 0 \\
0 & 0 & 0 & 0 & 0 & 0 & 0 & 0 & 0 & 0 & 0 & \frac{\beta_2 v}{\rho_2 \kappa} & 0 \\
0 & 0 & 0 & 0 & 0 & 0 & 0 & 0 & 0 & 0 & 0 & 0 & \frac{\beta_2 v}{\rho_2 \kappa}
\end{array}\right) \tag{A5}$$

Here, we have added the auxiliary variables

$$\begin{aligned}
\rho &= \phi\rho_F + (1-\phi)\rho_S,\\
m &= \rho_F T/\phi,\\
\rho_1 &= \rho - \rho_F^2/m,\\
\rho_2 &= \rho_F - m\rho/\rho_F,\\
\beta_1 &= \rho_f/m,\\
\beta_2 &= \rho/\rho_F.
\end{aligned} \tag{A6}$$

APPENDIX B: DETAILS OF THE POROELASTIC DYNAMIC RUPTURE SOLVER

We follow the ideas of de la Puente *et al.* (2009), Duru *et al.* (2021) and Uphoff (2020), who studied dynamic rupture in ADER-DG schemes, to derive the equations for dynamic rupture sources in poroelastic media. An even more detailed derivation can be found in (Wolf 2024).

The first task is to compute the state $\vec{Q}^*$ at the interface, based on the solution of a Riemann problem, that is, the states $\tilde{Q}^-$ and $\tilde{Q}^+$ are given as initial values on the left and the right, respectively. In the poroelastic case, we observe three wave types (P wave, S Wave slow P wave). Therefore, we observe a solution structure as in Fig. B1. The states $\vec{Q}^a$, $\vec{Q}^b$, $\vec{Q}^c$, $\vec{Q}^d$, $\vec{Q}^e$ and $\vec{Q}^f$ can be computed from the Rankine–Hugoniot relations, if we assume continuity of the normal stress, the fluid pressure, the solid velocities and the relative fluid velocity in normal direction at $x = 0$. The states at the interface are expressed as

$$\begin{aligned}
\vec{Q}^c - \tilde{Q}^- &= \alpha_1\vec{r}_1^- + \alpha_2\vec{r}_2^- + \alpha_3\vec{r}_3^- + \alpha_4\vec{r}_4^-\\
\tilde{Q}^+ - \vec{Q}^d &= \alpha_{10}\vec{r}_{10}^+ + \alpha_{11}\vec{r}_{11}^+ + \alpha_{12}\vec{r}_{12}^+ + \alpha_{13}\vec{r}_{13}^+,
\end{aligned} \tag{B1}$$

where α are coefficients and $\vec{r}$ are eigenvectors of the flux matrix A. The eigenvectors $\vec{r}_5, \vec{r}_6, \vec{r}_7, \vec{r}_8$ and $\vec{r}_9$ do not contribute to the solution of the Riemann problem, since their respective eigenvalues are all 0. We write down the eigenvectors in a 13×13 matrix and slice out four 4×4 matrices:

$R =$

	1	2	3	4	5	6	7	8	9	10	11	12	13
σ_{11}	*			*						*			*
σ_{22}	*			*	*					*			*
σ_{33}	*			*		*				*			*
σ_{13}		*										*	
σ_{23}							*						
σ_{13}			*								*		
u	*			*						*			*
v		*										*	
w			*								*		
p	*			*						*			*
u_f	*			*						*			*
v_f		*						*				*	
w_f			*						*		*		

. (B.2)

Here a $*$ denotes a non-zero entry. The matrices R_T^- and R_T^+ correspond to the traction values $\vec{T} = (\sigma_{11}\ \sigma_{12}\ \sigma_{13}\ p)^T$, whereas the matrices R_V^- and R_V^+ correspond to the velocity values $\vec{V} = (u\ v\ w\ u_f)^T$. In addition, we define $\vec{\alpha}^- = (\alpha_1\ \alpha_2\ \alpha_3\ \alpha_4)^T$ and $\vec{\alpha}^+ = (\alpha_{10}\ \alpha_{11}\ \alpha_{12}\ \alpha_{13})^T$. Now, we can write eq. (B1) as:

$$\begin{aligned}
\vec{T}^c - \tilde{T}^- &= R_T^-\vec{\alpha}^-, \qquad \vec{V}^c - \tilde{V}^- = R_V^-\vec{\alpha}^-,\\
\tilde{T}^+ - \vec{T}^d &= R_T^+\vec{\alpha}^+, \qquad \tilde{V}^+ - \vec{V}^d = R_V^+\vec{\alpha}^+.
\end{aligned} \tag{B3}$$

At a dynamic boundary interface, the traction parts are continuous: $\vec{T}^* = \vec{T}^c = \vec{T}^d$, but the tangential velocities can be discontinuous. Fault opening is not allowed in our model, thus $u^* = u^c = u^d$ and $u_f^* = u_f^c = u_f^d$. Based on the jump conditions, we can establish a relation that the

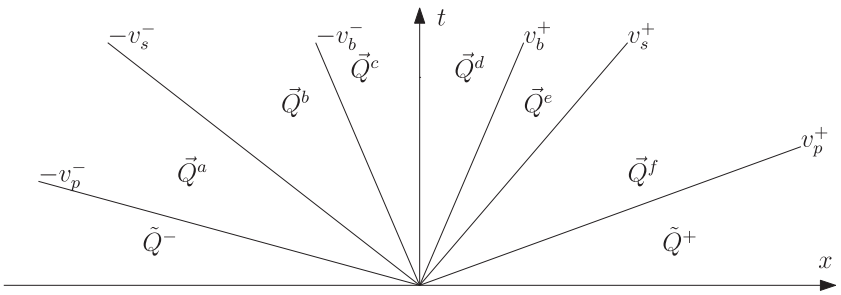

Figure B1. Solution structure of the poroelastic Riemann problem. In addition to the *P* and *S* waves, we also observe the slow *P* wave (subscript *b* for Biot). We observe left and right-hand states ($\tilde{Q}^-$, $\tilde{Q}^+$) and six intermediate states $\vec{Q}^a$, $\vec{Q}^b$, $\vec{Q}^c$, $\vec{Q}^d$, $\vec{Q}^e$, $\vec{Q}^f$, separated by the slow and fast *P* and the *S* waves.

traction at the interface and the slip rate have to fulfill. Uphoff (2020, eq. 4.50) has derived the formula for the elastic case. If we follow the same steps for the poroelastic case, we find:

$$\begin{aligned}\left[\!\left[\vec{V}^*\right]\!\right] &= \vec{V}^d - \vec{V}^c \\ &= \left(\tilde{V}^+ - R_V^+\vec{\alpha}^+\right) - \left(\tilde{V}^- + R_V^-\vec{\alpha}^-\right) \\ &= \tilde{V}^+ - \tilde{V}^- - R_V^+\left(R_T^+\right)^{-1}\left(\tilde{T}^+ - \vec{T}^d\right) - R_V^-\left(R_T^-\right)^{-1}\left(\vec{T}^c - \tilde{T}^-\right) \\ &= \tilde{V}^+ - \tilde{V}^- - R_V^+\left(R_T^+\right)^{-1}\tilde{T}^+ + R_V^-\left(R_T^-\right)^{-1}\tilde{T}^- \\ &+ \left(R_V^+\left(R_T^+\right)^{-1} - R_V^-\left(R_T^-\right)^{-1}\right)\vec{T}^*.\end{aligned} \tag{B4}$$

We define the matrices $\left(Z^\pm\right)^{-1} := R_V^\pm\left(R_T^\pm\right)^{-1}$ and $\eta^{-1} := R_V^-\left(R_T^-\right)^{-1} - R_V^+\left(R_T^+\right)^{-1}$. In analogy to eq. 4.50 in Uphoff (2020), we write:

$$\left[\!\left[\vec{V}^*\right]\!\right] = \left[\!\left[\tilde{V}\right]\!\right] - \left(Z^+\right)^{-1}\tilde{T}^+ + \left(Z^-\right)^{-1}\tilde{T}^- + \eta^{-1}\vec{T}^*. \tag{B5}$$

The structure of the involved matrix only couples u and u_f, but the tangential velocity components v and w are still independent as in the elastic case. Similar to the elastic case, we define

$$\vec{\Theta} := \eta\left(\left[\!\left[\tilde{V}\right]\!\right] - \left(Z^+\right)^{-1}\tilde{T}^+ + \left(Z^-\right)^{-1}\tilde{T}^-\right). \tag{B6}$$

This allows us to relate the tractions and velocities at the fault:

$$\eta\left[\!\left[\vec{V}^*\right]\!\right] + \vec{T}^* = \vec{\Theta}. \tag{B7}$$

Now, the task is to find velocities and tractions $\vec{V}^\mathrm{DR}$ and $\vec{T}^\mathrm{DR}$, which are consistent with the friction law and eq. (B7). We already have established continuity of u and u_f, thus $[\![u^\mathrm{DR}]\!] = 0$ and $\left[\!\left[u_\mathrm{f}^\mathrm{DR}\right]\!\right] = 0$. As a direct consequence, we obtain $\sigma_{11}^\mathrm{DR} = \Theta_1$ and $p^\mathrm{DR} = \Theta_4$. For the tangential parts of the traction, we have to solve a system of linear equations:

$$\begin{aligned}\tau\left[\!\left[V_2^\mathrm{DR}\right]\!\right] &= T_2^\mathrm{DR}\|\vec{s}\|, \quad \eta_{22}\left[\!\left[V_2^\mathrm{DR}\right]\!\right] + T_2^\mathrm{DR} = \Theta_2, \\ \tau\left[\!\left[V_3^\mathrm{DR}\right]\!\right] &= T_3^\mathrm{DR}\|\vec{s}\|, \quad \eta_{33}\left[\!\left[V_3^\mathrm{DR}\right]\!\right] + T_3^\mathrm{DR} = \Theta_3,\end{aligned} \tag{B8}$$

where η_{22} and η_{33} are coefficients of the matrix η. The fault strength $\tau(\|\vec{s}\|, \phi) = \mu_f(\|\vec{s}\|, \psi)\cdot\sigma_n$ depends on the friction parameter μ_f and the effective normal stress σ_n. Depending on the choice of friction law, the friction parameter depends on the slip rate $\|\vec{s}\|$ and the state variable ϕ. In the isotropic poroelastic case, the values η_{22} and η_{33} coincide. We define $\eta := \eta_{22} = \eta_{33}$. In the isotropic poroelastic case, the values η_{22} and η_{33} coincide. We recall that $\|\vec{s}\| = \sqrt{\left[\!\left[V_2^\mathrm{DR}\right]\!\right]^2 + \left[\!\left[V_3^\mathrm{DR}\right]\!\right]^2}$ and obtain the equation

$$\tau_S(\|\vec{s}\|, \phi) + \eta\|\vec{s}\| = \sqrt{\Theta_2^2 + \Theta_3^2}, \tag{B9}$$

which has to be solved for the slip rate $\|\vec{s}\|$.

We recall that the fluid pressure has a weakening effect on the fault: When computing the fault strength $\tau = \max\left(0, -\mu_f\tilde{\sigma_n} - C\right)$, we have to consider the augmented normal stress $\tilde{\sigma}_n = T_1 - p$. We use a Newton–Raphson solver to calculate the slip rate based on eq. (B9). Once the slip rate $\|\vec{s}\|$ is known, we compute its two components and the two tractions from eq. (B8). Now, the imposed state $\vec{T}^\mathrm{DR}$ and the slip rates $\left[\!\left[\vec{V}^\mathrm{DR}\right]\!\right]$ are known. We use eq. (B4) to compute $\vec{V}^c$ and $\vec{V}^d$. From eq. (B1), we conclude that we can compute $\vec{V}^c$ and $\vec{V}^d$ from $\tilde{V}^-$,

$\tilde{V}^+$ and $\vec{\alpha}^{\pm}$. The coefficients $\vec{\alpha}^{\pm}$ solely depend on the traction values $\vec{T}^c$, $\vec{T}^d$, $\tilde{T}^-$ and $\tilde{T}^+$, which are known at this time already. We conclude

$$\begin{aligned}
\vec{V}^c &= \tilde{V}^- + R_V^- \vec{\alpha}^- \\
&= \tilde{V}^- + R_V^- \left(R_T^-\right)^{-1} \left(\vec{T}^c - \tilde{T}^-\right) \\
&= \tilde{V}^- + \left(Z^-\right)^{-1} \left(\vec{T}^c - T^-\right) \\
\vec{V}^d &= \tilde{V}^+ - R_V^+ \vec{\alpha}^+ \\
&= \tilde{V}^+ - R_V^+ \left(R_T^+\right)^{-1} \left(\tilde{T}^+ - \vec{T}^d\right) \\
&= \tilde{V}^+ - \left(Z^+\right)^{-1} \left(\tilde{T}^+ - \vec{T}^d\right).
\end{aligned} \tag{B10}$$

With this equation, the states $\vec{Q}^c$ and $\vec{Q}^d$ are known. They are consistent with the Rankine–Hugoniot jump conditions as well as with the friction law. These states can now be used as imposed states at the interface to compute the upwind flux.

APPENDIX C: DETAILED SNAPSHOTS FOR THE FAULT BRANCHING SCENARIO

In this section, we show additional snapshots extending the information shown in Fig. 11.

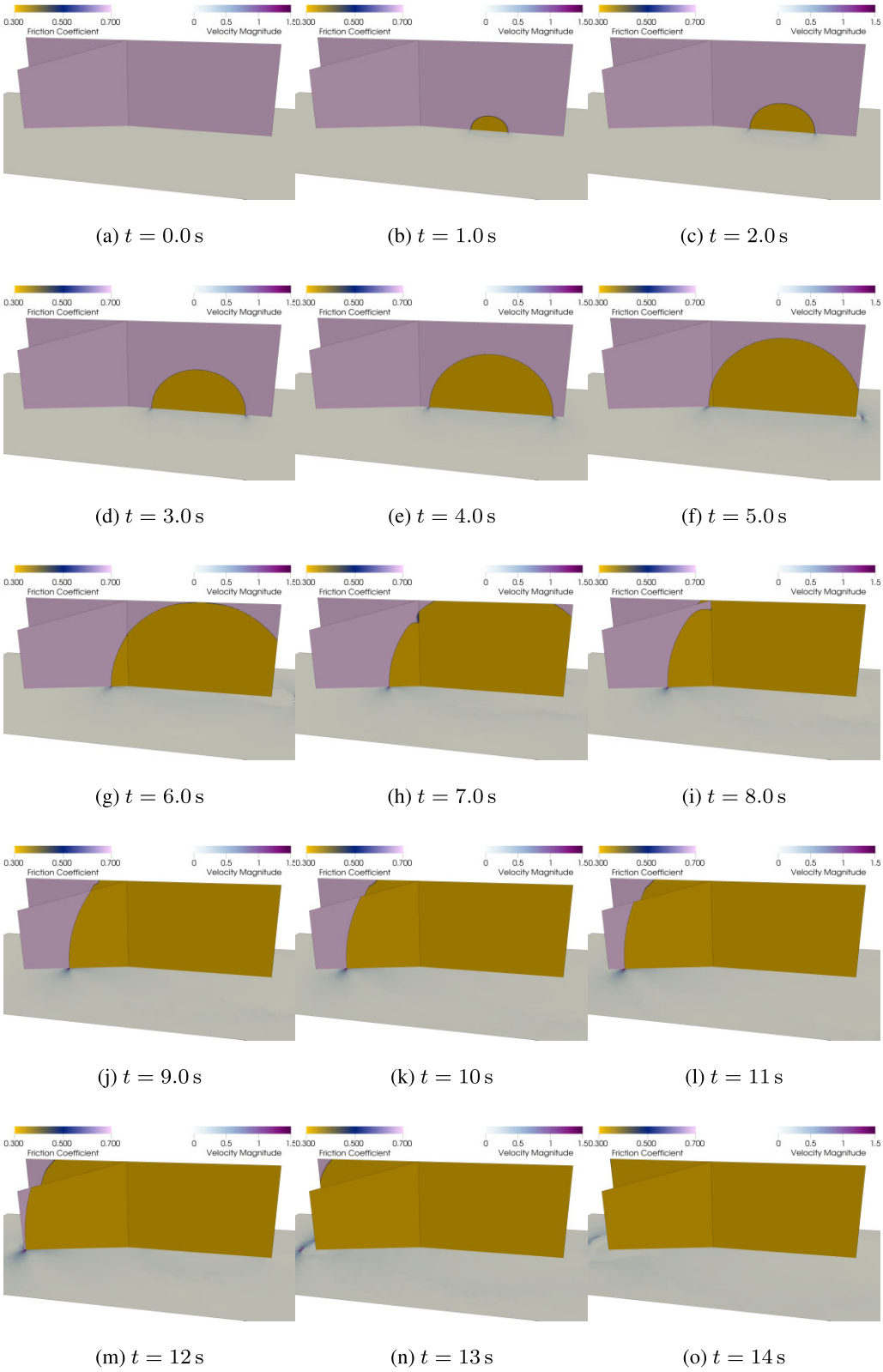

(a) $t = 0.0\,\mathrm{s}$ (b) $t = 1.0\,\mathrm{s}$ (c) $t = 2.0\,\mathrm{s}$

(d) $t = 3.0\,\mathrm{s}$ (e) $t = 4.0\,\mathrm{s}$ (f) $t = 5.0\,\mathrm{s}$

(g) $t = 6.0\,\mathrm{s}$ (h) $t = 7.0\,\mathrm{s}$ (i) $t = 8.0\,\mathrm{s}$

(j) $t = 9.0\,\mathrm{s}$ (k) $t = 10\,\mathrm{s}$ (l) $t = 11\,\mathrm{s}$

(m) $t = 12\,\mathrm{s}$ (n) $t = 13\,\mathrm{s}$ (o) $t = 14\,\mathrm{s}$

Figure C1. Time-series of the friction coefficient and wave field in the fault branching scenario for the poroelastic case with $\alpha = 0.9$. A more detailed movie of the rupture process is added as electronic supplement.

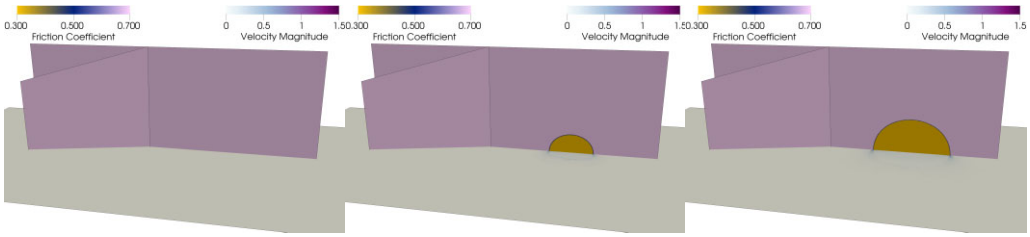

(a) $t = 0.0\,\mathrm{s}$ (b) $t = 1.0\,\mathrm{s}$ (c) $t = 2.0\,\mathrm{s}$

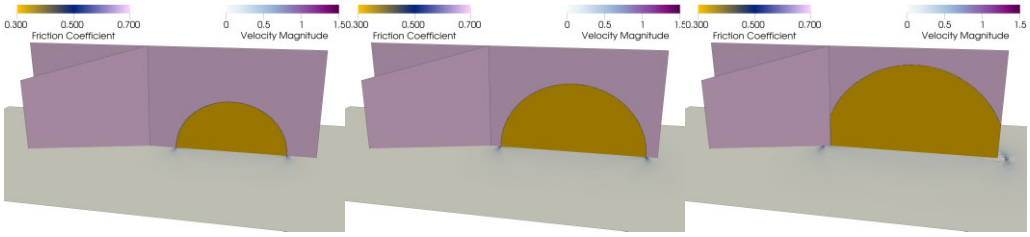

(d) $t = 3.0\,\mathrm{s}$ (e) $t = 4.0\,\mathrm{s}$ (f) $t = 5.0\,\mathrm{s}$

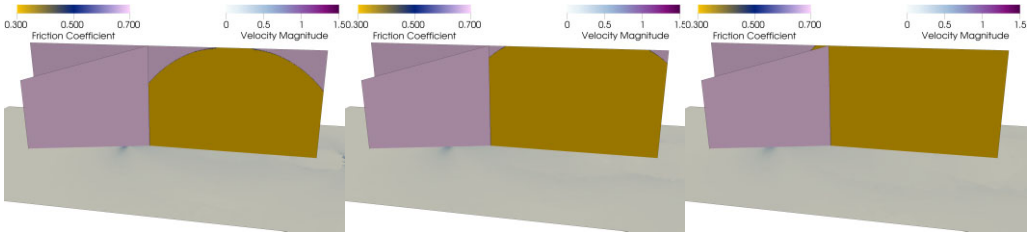

(g) $t = 6.0\,\mathrm{s}$ (h) $t = 7.0\,\mathrm{s}$ (i) $t = 8.0\,\mathrm{s}$

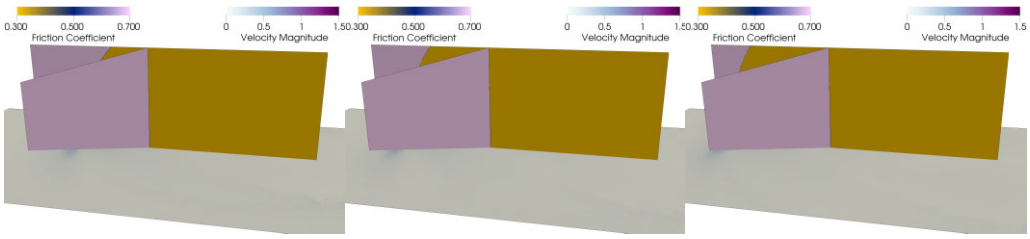

(j) $t = 9.0\,\mathrm{s}$ (k) $t = 10\,\mathrm{s}$ (l) $t = 11\,\mathrm{s}$

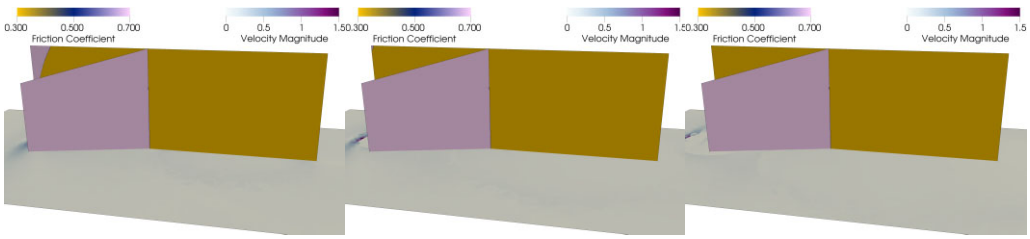

(m) $t = 12\,\mathrm{s}$ (n) $t = 13\,\mathrm{s}$ (o) $t = 14\,\mathrm{s}$

Figure C2. Time-series of the friction coefficient and wave field in the fault branching scenario for the Gassmann equivalent with $\alpha = 0.9$. A more detailed movie of the rupture process is added as electronic supplement.

APPENDIX D: MISFIT TABLES FOR THE HOMOGENEOUS FULL-SPACE TEST CASE

Table D1. Misfits at all receiver positions for the homogeneous full space, when the pores are filled with an inviscid fluid (all values in %).

Receiver	EM u	PM u	EM w	PM w	EM u_f	PM u_f	EM w_f	PM w_f
1	0.05	0.0	0.71	0.11	0.47	0.0	0.84	0.11
2	0.06	0.0	0.71	0.10	0.58	0.0	0.78	0.11
3	1.12	0.11	0.82	0.11	0.81	0.14	0.81	0.16
4	1.15	0.12	0.96	0.11	1.52	0.41	1.60	0.45
5	0.35	0.06	0.70	0.14	1.20	0.12	0.88	0.11
6	0.34	0.06	0.69	0.14	1.10	0.20	0.86	0.17
7	0.08	0.0	0.68	0.10	0.43	0.0	0.71	0.10
8	0.06	0.0	0.65	0.10	0.58	0.0	0.66	0.10
9	1.28	0.21	1.22	0.22	4.22	1.31	4.71	1.43
10	1.52	0.35	1.47	0.36	7.86	2.47	7.91	2.45
11	0.34	0.07	0.65	0.14	4.56	1.43	2.12	0.66
12	0.36	0.09	0.63	0.14	6.83	2.19	2.76	0.87

Table D2. Misfits at all receivers for the homogeneous full space scenario, when the pores are filled with a viscous fluid (all values in %).

Receiver	EM u	PM u	EM w	PM w	EM u_f	PM u_f	EM w_f	PM w_f
1	0.05	0.0	0.72	0.10	0.08	0.0	0.82	0.12
2	0.06	0.0	0.71	0.10	0.09	0.0	0.81	0.12
3	1.16	0.11	0.84	0.10	1.71	0.15	1.31	0.12
4	1.19	0.11	1.05	0.09	1.80	0.14	1.78	0.12
5	0.34	0.06	0.70	0.13	0.34	0.07	0.78	0.16
6	0.33	0.06	0.69	0.14	0.36	0.06	0.76	0.15
7	0.08	0.0	0.68	0.10	0.14	0.0	0.77	0.12
8	0.07	0.0	0.66	0.10	0.11	0.0	0.76	0.13
9	1.16	0.10	1.04	0.10	1.76	0.14	1.63	0.13
10	1.13	0.10	1.01	0.10	1.80	0.13	1.51	0.14
11	0.31	0.06	0.65	0.14	1.87	0.15	1.60	0.22
12	0.30	0.06	0.63	0.14	0.46	0.05	0.77	0.15